minerals

MDPI

Article

Facies, Depositional Environment and Reservoir Quality of an Early Cambrian Carbonate Ramp in the Tarim Basin, NW China

Yongjin Zhu [1,2], Jianfeng Zheng [1,2], Jiankun Zhang [3,4,*], Xinsheng Luo [5], Guang Yu [1], Jun Li [6], Fangjie Hu [5] and Guo Yang [5]

[1] PetroChina Hangzhou Institute of Geology, Hangzhou 310023, China; zhuyj_hz@petrochina.com.cn (Y.Z.); zhengjf_hz@petrochina.com.cn (J.Z.); yug_hz@petrochina.com.cn (G.Y.)
[2] PetroChina Key Laboratory of Carbonate Reservoir, Hangzhou 310023, China
[3] State Key Laboratory of Nuclear Resources and Environment, East China University of Technology, Nanchang 330013, China
[4] Jiangxi Engineering Technology Research Center of Nuclear Geoscience Data Science and System, East China University of Technology, Nanchang 330013, China
[5] PetroChina Tarim Oilfield Company, Korla 841000, China; luoxs-tlm@petrochina.com.cn (X.L.); hufangjie100@163.com (F.H.); yangguo-tlm@petrochina.com.cn (G.Y.)
[6] PetroChina Research Institute of Petroleum Exploration & Development, PetroChina, Beijing 100083, China; lijun69@petrochina.com.cn
* Correspondence: sparkler1984@126.com

Abstract: The Xiaoerbulake Formation in the Tarim Basin is considered one of the most important deep to ultradeep hydrocarbon reservoirs in the world. The objective of the present study is to analyze the facies, depositional environment and reservoir quality of the Early Cambrian Xiaoerbulake Formation in the Tarim Basin through integrated analysis of 120 m of cores, 3240 m of well cuttings, wireline logs and over 1100 thin sections from 17 exploration wells. Early Cambrian Xiaoerbulake Formation deposits in the Tarim Basin were deposited on a ramp setting. The ramp was occupied by seven facies associations and ten facies types ranging from the inner ramp to the outer ramp. These facies associations include tidal flat, lagoon, high-energy shoal, sabkha, inter-shoal, low-energy shoal and open shelf. Their distribution was controlled by paleogeographic patterns, sea level changes and the paleoclimate. Reservoir quality is considerably affected by facies together with diagenetic processes, including dolomitization and anhydrite cementation. High-quality reservoirs are found in the dolograinstone of high-energy shoal environments, which are favorable exploration facies in the carbonate ramp. Their pore space types consist of interparticle pores, intraparticle pores, intercrystalline pores, vuggy pores and moldic pores, with a porosity of 1.4%–7.5%. This study will help with our understanding of the stratigraphic framework, sedimentary-facies evolution and high-quality reservoir distribution of the Early Cambrian carbonate ramp in the Tarim Basin, facilitating exploration and the production of hydrocarbons from the Xiaoerbulake Formation.

Keywords: facies; depositional environments; reservoir quality; Xiaoerbulake Formation; Early Cambrian carbonate ramp; Tarim Basin

check for updates

Citation: Zhu, Y.; Zheng, J.; Zhang, J.; Luo, X.; Yu, G.; Li, J.; Hu, F.; Yang, G. Facies, Depositional Environment and Reservoir Quality of an Early Cambrian Carbonate Ramp in the Tarim Basin, NW China. *Minerals* **2023**, *13*, 791. https://doi.org/10.3390/min13060791

Academic Editors: Hamzeh Mehrabi, Vahid Tavakoli and Thomas Gentzis

Received: 9 May 2023
Revised: 4 June 2023
Accepted: 8 June 2023
Published: 10 June 2023

Copyright: © 2023 by the authors. Licensee MDPI, Basel, Switzerland. This article is an open access article distributed under the terms and conditions of the Creative Commons Attribution (CC BY) license (https://creativecommons.org/licenses/by/4.0/).

1. Introduction

The concept of carbonate ramps was established to characterize a very low-gradient sloping depositional surface (with a gradient < 1°) that passes gradually from a shallow, high-energy environment of offshore and downslope into a progressively deeper, lower-energy environment and ultimately into basinal facies [1,2]. Compared to the shelf model, carbonate ramps generally lack slope break belts that separate the shallow water areas from the basin [3]. They also differ from rimmed shelves as there are usually no continuous reef trends; high-energy lime sands situated close to the shoreline and clasts of shallow shelf-edge facies are generally not observed in deeper water breccias (if present) [2–4].

Based on the study of various types of carbonate platforms, ramps were subdivided into homoclinal and distally steepened ramps by [4]. Ramp deposits comprise the foundation phases for many large-scale carbonate platforms and occur as major basin fills in some structural and depositional settings. They also host a considerable number of petroleum and mineral deposits. Recently, with advancing carbonate hydrocarbon exploration and development, important oil and gas fields in connection with carbonate ramp deposits have been detected successively, such as the Early Carboniferous carbonate ramp of Brabant in Wales [5], the Lower Triassic Kangan Formation carbonate ramp of the South Pars Field in the Persian Gulf Superbasin [6], the carbonate ramp of the Early Cambrian Longwangmiao Formation in the Sichuan Basin [7], the Ordovician carbonate ramp of the Gucheng area and the Early Cambrian Xiaoerbulake Formation carbonate ramp in the Tazhong Uplift of the Tarim Basin [8]. Ramp-type carbonate platforms have attracted increasing attention [9,10] and have become favorable exploration targets. Despite their abundance and undoubted economic importance, the facies characteristics of Cambrian carbonate ramps and the relationships between facies and high-quality reservoirs are poorly understood.

The Middle–Early Cambrian sedimentary succession (540–513 Ma) of the Tarim Basin is configured with high-quality source rocks in the Early Cambrian Yuertusi Formation, large-scale dolostone reservoir rocks in the Early Cambrian Xiaoerbulake Formation and the Early Cambrian Wusongeer Formation and widespread seals of gypsum caprocks in the Middle Cambrian Shayilike Formation and the Awatage Formation. These favorable conditions for hydrocarbon accumulation enable this interval to be an important strategic replacement of deep to ultradeep oil and gas exploration [11]. The recent breakthroughs of Wells ZS1, LT1 and JNKT1 in the Cambrian subsalt dolostone have rendered the strata increasingly prominent for oil and gas exploration. The Xiaoerbulake Formation has become a key hydrocarbon exploration target in the Tarim Basin as the main horizon of the Early Cambrian subsalt dolostone [12]. However, deep to ultradeep carbonate rocks in China are characterized by old age, great burial depth (4600–8500 m) and long-term tectonic evolution [13]. The prototype basins are poorly preserved, and the distribution of high-energy facies zones is limited; therefore, exploration and development are impeded by huge technical and commercial risks. For example, Wells YL6, XH1, CT1 and HT2 failed successively (Figure 1a), calling into question the exploration direction and potential of deep to ultradeep carbonate rocks to a certain extent. The major theoretical and technical bottleneck is identifying whether to detect and finely describe the deep to ultradeep large-scale high-quality reservoirs [11,14,15]. Global case studies show that the distribution of large-scale carbonate reservoirs is mostly facies-controlled [6,10,16,17]. Therefore, an accurate determination of facies types and the distribution of facies is the key to predict high-quality reservoirs in the deep to ultradeep Xiaoerbulake Formation in the Tarim Basin. Economic interest has driven increased research into the sedimentary facies of the Early Cambrian Xiaoerbulake Formation in the Tarim Basin. Researchers have proposed that the Xiaoerbulake Formation belongs to the sedimentary facies zone of ramp, ramp–tidal flat, restricted platform, semi-evaporative platform, open platform margin or slope–basin [14,18–21]. However, previous studies mainly focused on limited well logging and cutting data and low-resolution 2D and 3D seismic data, but did not thoroughly address with the facies and facies associations of the Early Cambrian Xiaoerbulake Formation carbonate ramp. There is no fine characterization of the facies. To date, intensive research has not been conducted on the types and characteristics of the ramp facies and their impacts on favorable reservoirs. Thus, this will restrict the further exploration of the Early Cambrian subsalt dolostone in the Tarim Basin.

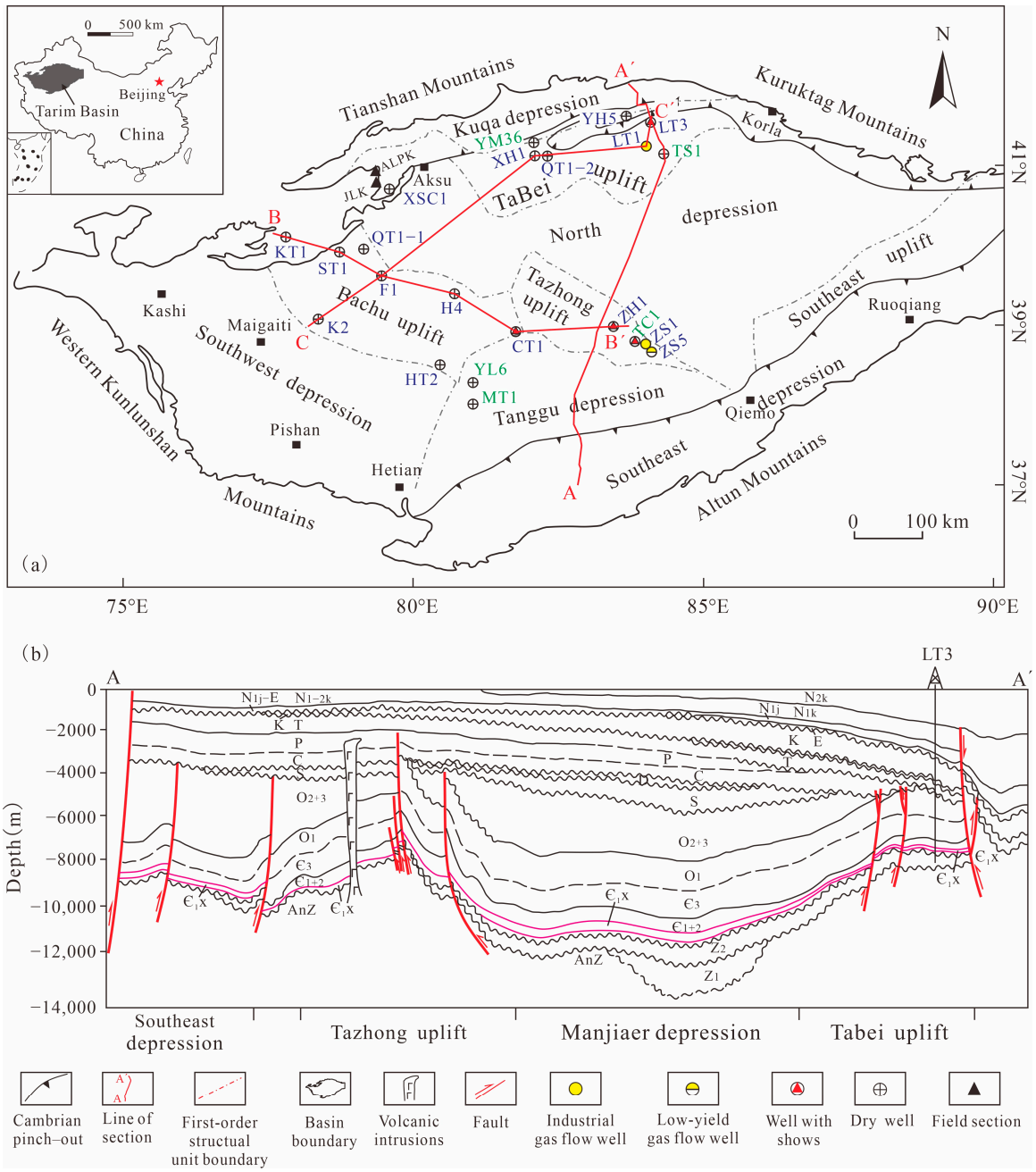


Figure 1. (**a**) Schematic tectonic provinces in the Tarim Basin (adapted from [22]); (**b**) Structural−stratal configuration section in the north−south direction (A−A′) (adapted from [23]. AnZ: Ediacaran; Z_2q: Qigebulake Formation; $\in_1y$: Yuertusi Formation; $\in_1x$: Xiaoerbulake Formation; $\in 1x_1^1$: the first member of the Lower Xiaoerbulake Formation; $\in_1w$: Wusongeer Formation; $\in_2s$: Shayilike Formation; $\in_2a$: Awatage Formation; O_1: Lower Ordovician; O_{2+3}: Mid−upper Ordovician; S: Silurian; C: Carboniferous; P: Permian; K, T: Jurassic and Triassic; E: Eocene; N: Neogene. Exploration wells (well names in blue) of the Lower Cambrian: KT1: Well Ketan1; ST1: Well Shutan1; QT1−1: Well Qiaotan1; K2: Well Kang2; F1: Well Fang1; HT2: Well Hetian2; H4: Well He4; CT1: Well Chutan1; ZH1: Well Zhonghan1; ZS1: Well Zhongshen1; ZS5: Well Zhongshen5; XSC1: Well Xinsucan1; XH1: Well Xinhe1; QT1−2: Well Qitan1; YH5: Well Yaha5; LT1: Well Luntan1; LT3: Well Luntan3. Exploration wells (well names in green) of the Early Cambrian Sayilike Formation and Awatage Formation: YL6: Well Yulong6; MT1: Matan1; TC1: Well Tacan1; YM36: Well Yingmai36; TS1: Well Tashen1. ALPK: Aolinpike section; JLK: Jinlinkuang section. Thickness data of field sections from [14].

Based on sedimentological methods, this study systematically analyzes the facies, depositional environment and reservoir quality of an Early Cambrian carbonate ramp in the Tarim Basin using drilling, core, cutting and well logging data. The aim of this paper is to (1) reveal facies and facies association characteristics; (2) establish a facies model; (3) discuss the controlling factors of facies and facies associations; (4) clarify high-quality reservoirs and (5) explore the relationship between facies and high-quality reservoirs in an Early Cambrian carbonate ramp in the Tarim Basin.

2. Geological Setting

The Tarim Basin is located in the south of the Xinjiang Uygur Autonomous Region of Northwest (NW) China. With an area of 56×10^4 km^2, the Tarim Basin is the largest inland petroliferous superimposed basin developed on the Archean–Early Mesoproterozoic metamorphic crystalline basement and metamorphic fold basement. The Tarim Basin has experienced several periods of major structural changes during its formation and evolution, which gave rise to the present tectonic pattern of "four uplifts and five depressions" surrounded by mountains of the basin margin. The mountains include the Tianshan Mountains to the northwest, the Kuruktag Mountains to the southeast, the Kunlun Mountains to the southwest and the Altun Mountains to the southeast. The "four uplifts" are the Tabei Uplift, Bachu Uplift, Tazhong Uplift and Southeast Uplift. The "five depressions" are the Kuqa Depression, North Depression, Tanggu Depression, Southeast Depression and Southwest Depression (Figure 1a).

The Tarim Basin has undergone multiple periods of subsidence and uplift [24]. From the Early Cryogenian to the Early Paleozoic, influenced by aggregation and breakup events on the Rodinia supercontinent and the Gondwana continent, the Tarim Basin experienced strong regional extensional tectonic movements, which led to the formation of a unified paleo–Tarim plate. In the late Ediacaran, the Tarim Basin entered the rift–depression transition stage of the ancient rift system from the rift stage owing to mantle bulge, crustal attenuation or extension (Figure 1b). In addition to local synsedimentary faults, the basin was dominated by thermal subsidence and demonstrated differential characteristics, namely "uplift in the south and platform in the north, high in the south and low in the north" [14,25]. At the end of Ediacaran, the Cryogenian–Ediacaran Formations in the whole basin were denuded to varying degrees, while a regional large-scale unconformity between Ediacaran Formations and Cambrian Formations was generated owing to the Keping movement [26]. From the Early Cambrian to the Middle Cambrian, the post-rift subsidence stage and construction stage of the craton occurred under an extensional background in the Tarim Basin (Figure 2). In addition to the late Ediacaran differentiation characteristics of "north–south differentiation, structural high in the south and structural low in the north", the basin exhibited a new characteristic of "structural high in the west and structural low in the east" [27].

The Cryogenian–Middle Cambrian sedimentary succession of the Tarim Basin has been extensively studied, mostly through drilling data for hydrocarbon exploration [12,14,19,25,28]. The Cryogenian–Ediacaran sedimentary succession in the Tarim Basin was deposited with extremely thick coarse clastic deposits interbedded with mudstone and carbonate rocks, multiple sets of volcanic extrusive rocks, intrusive rocks and four sets of lodgement till deposits. These deposits recorded the tectono–sedimentary response from the initial rifting stage to the main rifting stage. The Early–Middle Cambrian sedimentary succession includes the Early Cambrian Yuertusi, Xiaoerbulake and Wusonggeer Formations and the Middle Cambrian Shayilike and Awatage Formations, which were revealed in the drilling results from 22 exploration wells (Figures 1a and 2). The sediments in the Tarim Basin were restricted by the paleogeographic framework with three paleohighs (Uqia, Tanan and Keping–Wensu) and two depressions (southwestern Tarim Depression and North Depression) in the Early Cambrian. The Yurtusi Formation was clearly controlled by the Precambrian tectonic framework of the alternated uplifts and depressions, and has a sediment thickness of 8–70 m. A set of diamictite rocks can be observed in the Bachu Uplift, and

the Tabei Uplift is dominated by black bioclastic mudstone, siliceous mudstone and muddy limestone interbedded with thin-bedded dolostone, which are favorable source rocks. The Xiaoerbulake Formation comprises a set of carbonate ramp deposits with a thickness ranging from 38 m to 372 m. According to the drilling results of Wells ZS1, ZH1, CT1, QT1–2 and KT1, in the southeast of the Tazhong Uplift, the Bachu Uplift and the northern margin of the Tanggu Depression, the formation is mainly characterized by terrigenous diamictite sediment, peloidal algal dolostone and dolostone with a set of diamictite and muddy dolostone in the middle part and anhydrite–salt rock and local volcanic rock intrusions. The upper part evolves into a set of argillaceous limestone and marl deposits in the QT1–1 well block of the Bachu Uplift. In the Tabei Uplift, represented by Wells XH1, LT1, LT3 and QT1–2, the lower part of the Xiaoerbulake Formation mainly comprises medium–thick-bedded dark gray (muddy) dolomitic or dolostone-bearing limestone, algal limestone and peloidal micritic limestone, while the upper part is mainly composed of (mud-bearing) peloidal or fine-grained dolomitic limestone and bioclastic (dolomitic) limestone. The lithologic associations of thick-bedded dolostone interbedded with thin-bedded algal dolostone are well developed in the local well blocks such as the YH5 well block of the Tabei Uplift. The Wusonggeer Formation has a thickness ranging from 32 m to 423 m. Argillaceous or terrigenous clastic dolostones interbedded with algal dolostone, dolomitic mudstone, gypsiferous rocks and local intrusive rocks were recorded in wells QT1–1, K2, HT2 and ZS1 in the Bachu Uplift, Tanggu Depression and Tazhong Depression. In the Tabei Uplift, the lower part of the Wusonggeer Formation in Well XH1 and Well LT1 mainly comprises a set of thick-bedded (dolostone-bearing) peloidal or fine-grained limestone with thin-bedded marl and (mud-bearing) dolomitic limestone. The middle–upper part in Wells LT3, TS1 and LT1 consists of thick-bedded peloidal dolostone, (mud-bearing) calcareous dolostone or dolomitic limestone. This set of formations is missing in the QT1–2 well block owing to the presence of a submarine uplift in the Tabei Uplift. The Shayilike and Awatage Formations are characterized by extensive thick anhydrite–salt rock and anhydritic dolostone with thicknesses of 48–459 m and 158–494 m, reflecting the sedimentary environment of strongly rimmed platforms dominated by evaporative lagoons under the prolonged hot arid paleoclimate.

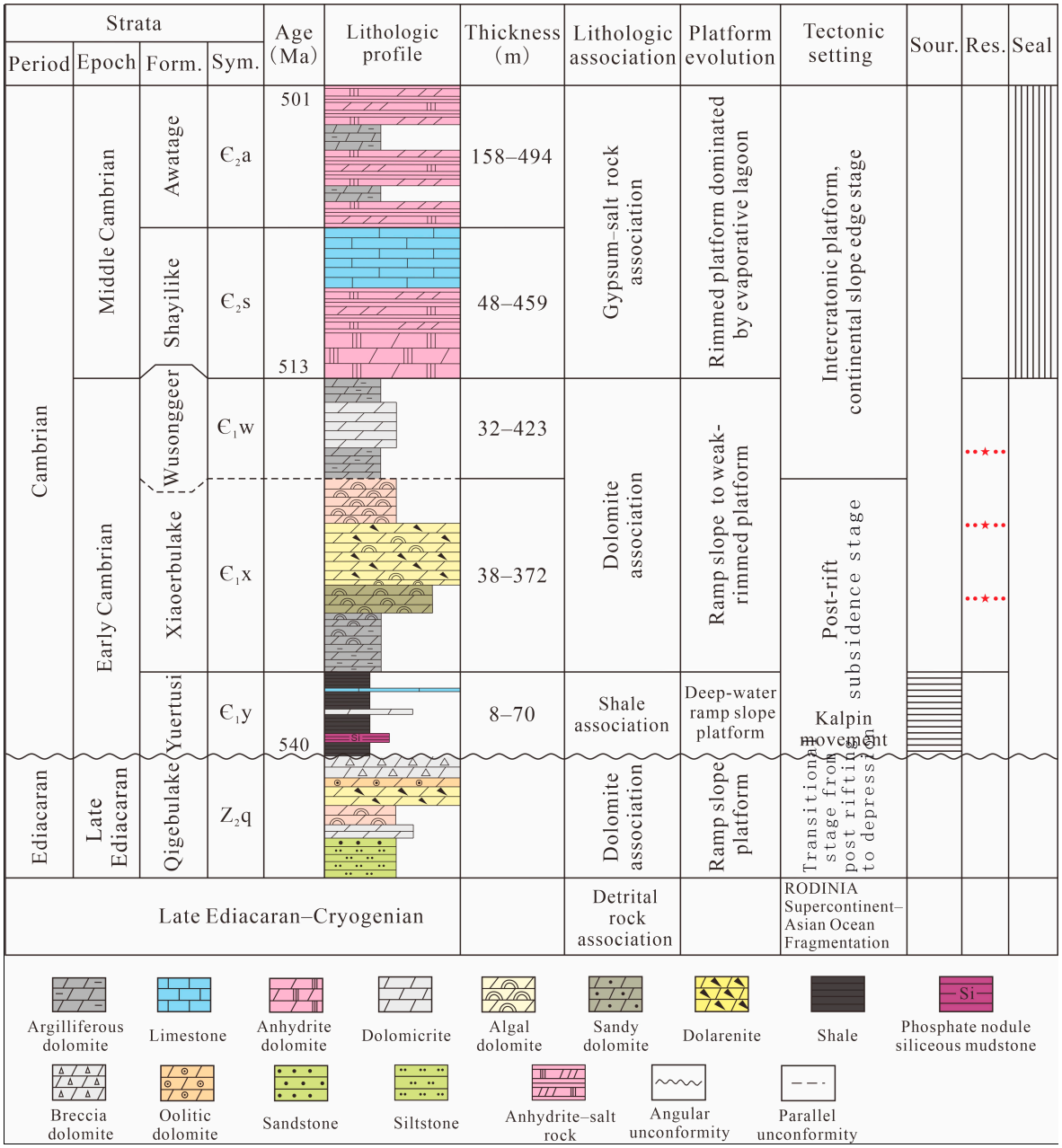


Figure 2. Generalized stratigraphic column (adapted from [11]). Age data from [29,30]. The thickness data are derived from the 17 exploration wells shown in Figure 1a.

3. Materials and Methods

A combination of 120 m of cores, 3240 m of cuttings and wireline logs from 17 wells were used to study the facies and to present a sedimentary model of the Early Cambrian Xiaoerbulake Formation in the Tarim Basin (Table 1). Over 1100 thin sections were prepared from the core and cutting samples collected at intervals of 2–5 m and at each lithological change in each well. The cores, cuttings and drilling data were provided by the Exploration and Development Research Institute of PetroChina Tarim Oilfield Company in Korla, Bayingolin Mongolian Autonomous Prefecture, Xinjiang Uyghur Autonomous Region, Northwest China. These thin sections were stained with alizarin red S and observed and photographed using a Leica DM2500 transmitted and reflected polarizing microscope. Over 12,000 photographs of the representative lithologic characteristics were obtained. The facies characteristics, such as the lithology (studied in terms of bedding, color, grain size,

proportions of grains and amount of mud), thickness, grain types, fossils, and depositional textures, were studied in detail.

Table 1. Core and cuttings information, thickness and depth of the Early Cambrian Xiaoerbulake Formation from 17 wells.

Well	Thickness (m)	Depth (m)	Sampling Depth of Cuttings (m)	Length of Cuttings (m)	Coring Depth (m)	Core Length (m)	Core Recovery (%)
ZH1	109	7381–7490	7381–7490	109	7356.9–7369.8 7387.5–7391.5 7400–7413 7473.69–7480.85	12.74 2.68 8.66 7.16	98.8 67 70.6 100
XH1	372	7420–7792	7420–7792	372	7473.69–7480.85	7.16	100
ZS1	49.85	6760.65–6810.5	6760.65–6810.5	49.85	6804–6807.36	2.62	78
YH5	273.8	6023.48–6297.28	6023.48–6297.28	273.8	6023.48–6025 6122.2–6127.2 6240.86–6246.26	1.52 5 5.4	100 100 100
LT3	160.45	8343–8503.45	8343–8503.45	160.45	8370–8378	7.99	99.9
F1	204.85	4409.15–4614	4409.15–4614	204.85	4513.1–4520.25 4579.63–4582.53	7.15 2.9	100 100
QT1−1	210	5860–6070	5860–6070	210	6006–6013	7	100
HT2	74.5	6460.5–6535	6460.5–6535	74.5	6492.12–6500.12	8	100
K2	195.65	5438.85–5634.5	5438.85–5634.5	195.65	5490.2–5497.2 5630.61–5634.5	6.6 3	94.3 77.1
ST1	188.2	1871.8–2000	1871.8–2000	188.2	1883–1889.3 1915–1919.43 1988.67–1996	5.98 4.3 7.29	94.9 97.1 99.5
KT1	212	4692–4904	4692–4904	212	4895.48–4903.48	7	87.5
XSC1	221.5	4852.5–5074	4852.5–5074	221.5	No coring		
CT1	71.15	7725.85–7797	7725.85–7797	71.15			
H4	140.8	5669.2–5810	5669.2–5810	140.8			
QT1−2	356.05	5600.3–5956.35	5600.3–5956.35	356.05			
ZS5	37.87	6749.5–6787.37	6749.5–6787.37	37.87			
LT1	363	8260–8623	8260–8623	363			

To interpret the paleoenvironment, we first created a lithologic description presenting different lithotypes, including color, thickness and sedimentary structures such as lamination and bioturbation and vertical and lateral distribution of individual lithofacies types and cycles. Subsequently, we determined the arrangement of the lithofacies types and conducted facies and facies association analyses. The classifications of carbonate rocks and mixed siliciclastic–carbonate rocks were conducted according to the nomenclature of [31–33]. Classification and descriptive terms for crystallization textures and crystallization fabrics of dolostone were provided by [33–35]. Carbonate platforms and carbonate ramp depositional systems developed by [1,4,33,36] were referred to for the sedimentary models of the Early Cambrian Xiaoerbulake Formation.

To investigate the main factors controlling reservoir quality, we first characterized the pore system such as space types and physical properties using thin sections and the porosity of log interpretation. Thin-section samples were impregnated with blue or pink epoxy to facilitate the recognition of porosity. Then, we investigated the diagenesis associated with the pore system of hydrocarbon reservoirs through thin sections and casting thin sections of well cuttings and drill cores. The porosity was computed using acoustic, neutron and density logs. The pore type classification developed here is based on the classification systems of [37].

4. Results

4.1. Facies Analysis

Based on the depositional attributes and textural constituents, ten types of facies were recognized in the Early Cambrian Xiaoerbulake Formation in the Tarim Basin. They were

further grouped into seven facies associations (FA1–FA7; Table 2) and twenty-six main types of facies associations were present (TFA1–TFA26; Table 2).

Table 2. Facies, facies association and depositional environment of an Early Cambrian carbonate ramp in the Tarim Basin, NW China.

Facies Association (FA)	Type of Facies Association (TFA)	Facies Type	Well	Depositional Environment
Tidal flat facies association (FA1)	Thick-bedded sandy dolostone (TFA1). Dolomitic sandstone with thin interlayer of argillaceous rock (TFA2). Sandstone and dolomitic sandstone with thin interlayer of mudrock (TFA3).	Mixed siliciclastic–carbonate rock (F1)	ZS1 and ZH1 KT1 ZH1	Inner ramp
	Medium- to thick-bedded dolostone (TFA4). Medium-bedded dolostone with thin interlayers of argillaceous dolostone (TFA5). Dolostone with interbedded thin layers of oolitic dolostone and anhydrite-bearing dolostone (TFA6).	Crystalline dolostone (F2)	YH5, ST1, QT1–1, ZS1, ZH1, K2 and H4 ZS1, ZS5 CT1	
	Dolomitized stromatolite interbedded with medium–thin interlayers of argillaceous dolostone (TFA7). Medium- to thick-bedded dolomitized stromatolite (TFA8).	Dolobindstone (F3)	YH5 YH5, ST1 and K2	
Lagoon facies association (FA2)	Argillaceous dolostone and dolomicrite with medium–thin interlayers of dolostone (TFA9).	Dolomudstone (F4)	F1 and ZH1	
	Mud-bearing limestone interbedded with dolomicrite and argillaceous limestone (TFA10). Dolostone, limy dolostone and dolomite-bearing limestone with thin interlayers of mudrock and silt-bearing argillaceous dolostone (TFA11).	Argillaceous dolostone (F5)	QT1–1 ST1 and QT1–1	
High-energy shoal facies association (FA3)	Sand-bearing dolarenite and oolitic dolostone with thin interlayer of dolostone (TFA12). Dolarenite and oolitic dolostone interbedded with dolostone (TFA13). Thrombolites and algal lumps (TFA14).	Dolograinstone (F6)	CT1 CT1, ZH1, ZS1 and H4 KT1 and ST1	
High-energy shoal facies association (FA3)	Dolarenite with thin interlayers of algal dolostone (TFA15). Dolarenite and oolitic dolostone with thin interlayers of algal dolostone (TFA16). Algal dolostone interbedded with oolitic dolostone, dolarenite and grain dolostone (TFA17).	Dolograinstone (F6)	F1 CT1 K2	Inner ramp
Sabkha facies association (FA4)	Anhydrite–salt rock with thin–medium interlayers of anhydritic dolostone (TFA18). Anhydritic dolostone with thin interlayers of anhydrite–salt rock (TFA19).	Anhydrite–salt rock (F7)	K2 H4 and K2	
Inter-shoal facies association (FA5)	Medium- to thick-bedded dolomite-bearing limestone with thin to medium interlayers of mud-bearing limestone (TFA20). Thick-bedded dolomite-bearing limestone (TFA21). Dolostone, limestone and dolomite-bearing limestone with argillaceous limestone interbed (TFA22).	Microcrystalline limestone (F8)	QT1–2, XSC1 and LT3 YH5, XSC1 and LT1 QT1–2	Mid-ramp
Low-energy shoal facies association(FA6)	Dolomite-bearing limestone, dolomitic limestone and limestone interbedded with thin-bedded peloidal dolomite-bearing limestone (TFA23). Medium–thick-bedded peloidal dolomite-bearing limestone (with peloidal dolomitic limestone and peloidal liny dolostone) (TFA24).	Peloidal grainstone (F9)	XH1 and LT1 QT1–2, LT1 and LT3	
Open-shelf facies association (FA7)	Thick-bedded mud-bearing limestone with thin interlayers of argillaceous limestone and dolomite-bearing limestone (TFA25). Dolomite-bearing limestone and mud-bearing limestone with thin interlayers of argillaceous limestone (TFA26).	Argillaceous limestone (F10)	QT1–2 and LT3 XH1	Outer ramp

Note that the terms of thick-bedded, medium-bedded and thin-bedded are determined by the relative thickness of lithotypes in TFA.

4.1.1. Mixed Siliciclastic–Carbonate Rock (F1)

Description: F1 mainly comprises sandy dolostone (Figure 3A,B), dolomitic sandstone (Figure 3C) and sandstone (Figure 3D). Sandy dolostone is generally gray in color and 6.6 m to over 19 m thick. Microscopically, it dominantly comprises dolomite and quartz, with a small amount of bitumen (Figure 3A) or argillaceous materials filling intercrystalline pores. The dolomite crystals are silt-sized to finely crystalline (<0.25 mm) and are characterized by inequigranular texture and hypidiotopic and idiotopic fabric. The concentration of quartz grains that are embedded in dolomite crystals accounts for 25%–35% of the total compo-

sition. The grains are moderately sorted, predominantly angular and mostly silt-sized to medium sand (0.04–0.3 mm in size). Dolomitic sandstone is gray to dark gray in color and 3–9 m thick. Microscopically, this lithotype mainly consists of silicified quartz and dolomite. Quartz grains are poorly sorted and angular. Furthermore, their size is fine to medium sand (0.1–0.3 mm), exhibiting monocrystalline and polycrystalline structures. Most quartz grain margins were dissolved (Figure 3C). Dolomite is microcrystalline in size. Quartz sandstone is commonly light gray to gray in color and ~8 m thick. Microscopically, this lithotype includes quartz, bituminous and dolomicritic matrix and glauconite (Figure 3D). Quartz grains are moderately sorted, and most of them are smaller than 0.1 mm, while medium or coarse-sized grains > 0.4 mm can be observed sporadically. Silt-sized quartz grains are mainly angular, and sand-sized quartz grains are rounded, mainly elliptical in shape. Siliciclastic sediments in the study area mainly occurred in the lower part of the Xiaoerbulake Formation adjoining the Southern Tarim Paleohigh and Wuqia Paleohigh [25].

F1 is present in TFA1–TFA3 (Table 2; Figure 4A–C). TFA1 occurs in the middle part of the Xiaoerbulake Formation in the ZS1 well block and the upper part of the Xiaoerbulake Formation in the ZH1 well block in the Tazhong Uplift. TFA2 mainly occurs at the base of the Xiaoerbulake Formation in the KT1 well block in the Keping Uplift, with a thickness of 18 m. It comprises dolomitic fine sandstone, dolomitic medium sandstone, dolomitic siltstone and argillaceous siltstone with thin interlayers of argillaceous rock. TFA3 is found at the base of the Xiaoerbulake Formation in the ZH1 well block in the Tazhong Uplift, with a thickness of up to 40 m. It is made up of thin interlayers of fine sandstone, siltstone, dolomitic siltstone, argillaceous dolomitic siltstone, argillaceous siltstone and mudrock. Vertically, fine sandstone, siltstone, dolomitic siltstone, argillaceous dolomitic siltstone and argillaceous siltstone form rhythmic superposition. TFA2 and TFA3 are packaged in upward-fining transgressive systems, tracting and draping over underlying Precambrian metamorphic basement rock of the paleohighs with a regional angle unconformity surface [25].

Interpretation: Mixed siliciclastic–carbonate sedimentation is related to paleo-environ mental conditions, such as paleoclimate and eustatic sea level change [38]. According to paleoclimate data reported by [39], siliciclastic sedimentation likely prevailed during the relatively hot and humid period, then palaeoclimatic conditions became more arid, favoring the deposition of carbonate [40] and evaporitic sediments [41]. This finding indicates that the early sedimentary period of the Xiaoerbulake Formation could have been a hot and humid climate in which siliciclastic sedimentation predominated. The middle sedimentary period of the Xiaoerbulake Formation might have evolved into an arid climate in which thick-bedded anhydrite–salt rock was formed in the middle part of the Xiaoerbulake Formation, as can be observed in some areas such as the K2 and H4 well blocks. The poorly sorted and angular siliciclastic grains in F1 suggest limited abrasion during transport, possibly reflecting a short transport to the tidal flat environments of the carbonate inner ramp from paleohighs by rivers [33,42]. The participation of airborne transport, however, cannot be excluded [42,43].

4.1.2. Crystalline Dolostone (F2)

Description: F2 is generally gray to dark gray in color and medium-bedded or thick-bedded (5 m to nearly 100 m thick). It mainly comprises silt-sized crystalline dolostone (Figure 3E), finely crystalline dolostone (Figure 3F,G) and medium crystalline dolostone (Figure 3H). Silt-sized crystalline dolostone and medium crystalline dolostone commonly occur in the Early Cambrian Xiaoerbulake Formation in the Tarim Basin, while medium crystalline dolostone is rarely observed. Microscopically, F2 is characterized by tightly packed inequigranular, mosaic, nonrhombic, anhedral and subhedral dolomite crystals exhibiting lobate and straight boundaries. The grain sizes of crystals vary from 0.04 mm to 0.3 mm. Intercrystalline pores are usually infilled with anhydrite (Figure 3F), with amounts ranging from 10% to 20%.

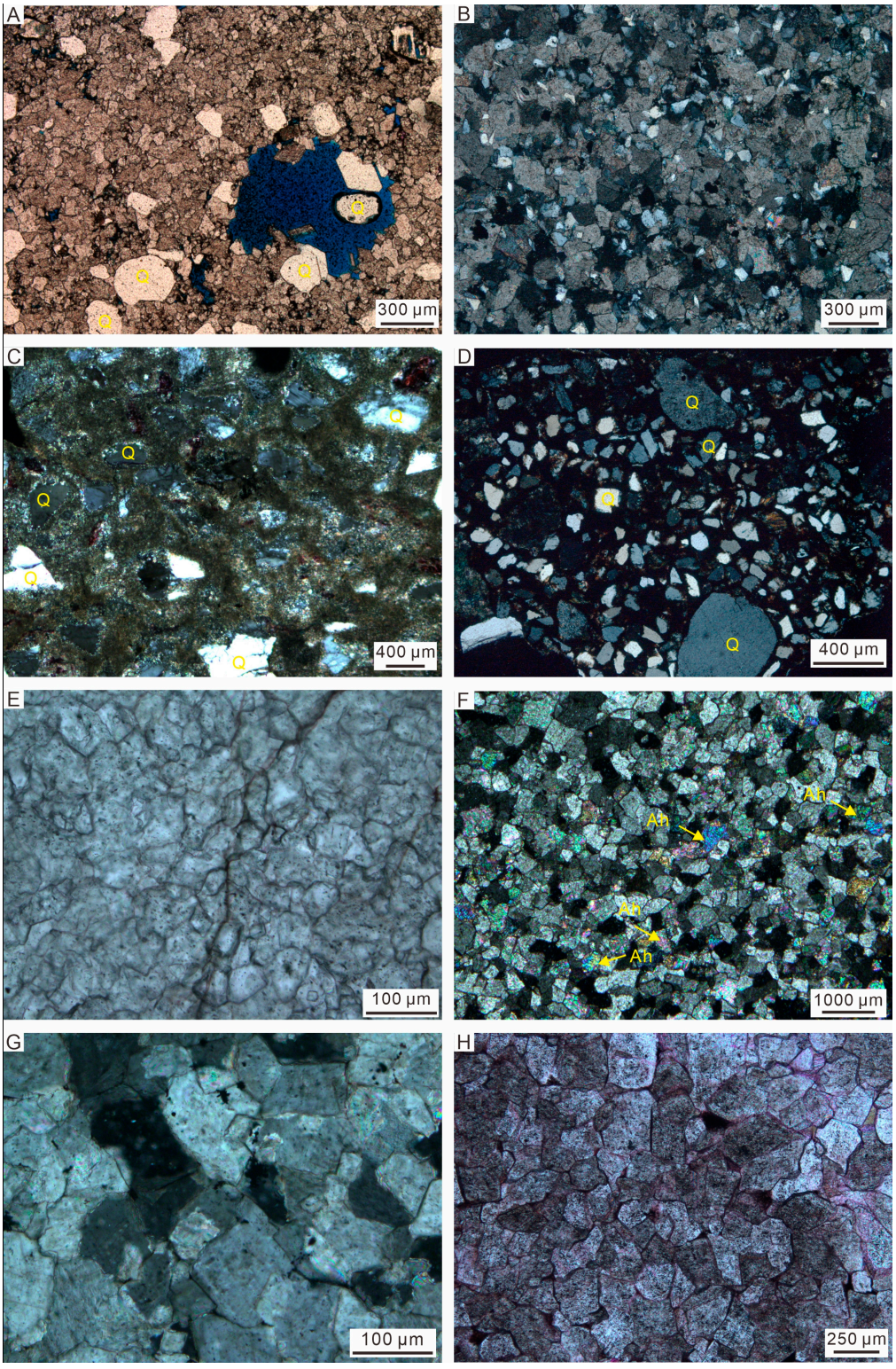


Figure 3. Photomicrographs of FA1 of the Early Cambrian Xiaoerbulake Formation in the Tarim Basin, Northwest China. (**A**) Sandy dolostone with subangular quartz grains, Well ZH1, depth 7387.5 m. (**B**) Silty dolostone, Well ZH1, depth 7479 m. (**C**) Dolomitic sandstone, Well KT1, 4900 m. (**D**) Bituminous sandstone, Well ZH1, 7484 m. (**E**) Silt-sized crystalline dolostone, Well CT1, depth 7794 m. (**F**) Finely crystalline dolostone with anhydrite, Well HT2, depth 6525 m. (**G**) Finely crystalline dolostone, Well HT2, depth 6525 m. (**H**) Medium crystalline dolostone, Well ST1, 1990.7 m. Q: grain; Ah: anhydrite.

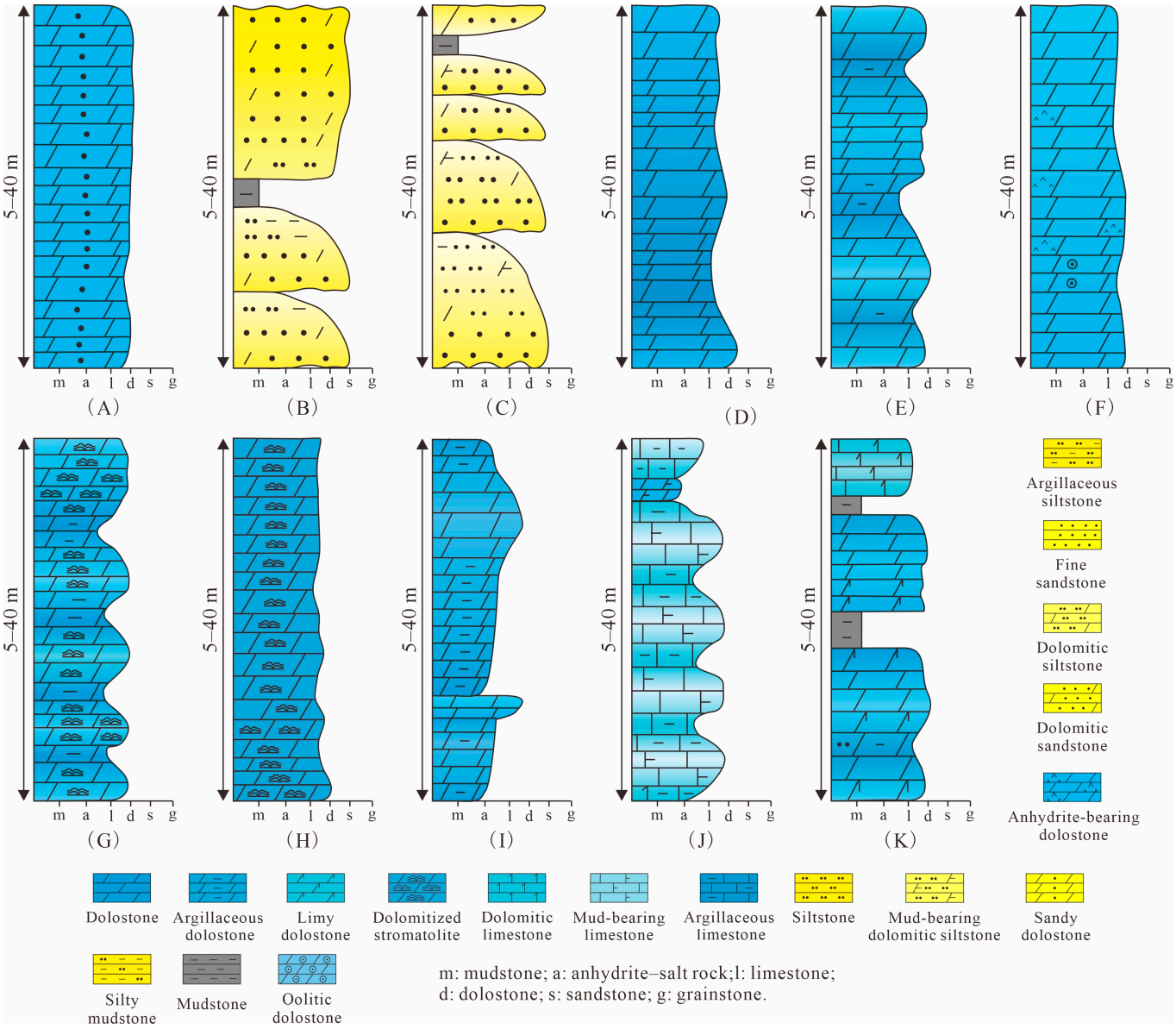


Figure 4. TFA1-10 of FA1 and FA2 of the Early Cambrian Xiaoerbulake Formation in the Tarim Basin, Northwest China. (**A**) TFA1; (**B**) TFA2; (**C**) TFA3; (**D**) TFA4; (**E**) TFA5; (**F**) TFA6; (**G**) TFA7; (**H**) TFA8; (**I**) TFA9; (**J**) TFA10; (**K**) TFA11.

This facies is present in TFA4, TFA5 and TFA6 (Table 2; Figure 4D–F). TFA4 is 5–100 m thick and better developed in the middle and upper part of the Xiaoerbulake Formation of the Keping Uplift, Bachu Uplift and Tazhong Uplift and the north of the Tabei Uplift, represented by Wells KT1, ST1, H4, QT1–1, K2, F1, ZS1, ZH1 and YH5. TFA5 is 5–10 m thick and is characterized by one to three sets of thin interlayers (0.9–2 m thick). This type of facies association is mainly found in the ST1, YH5 and ZH5 well blocks. TFA6 is developed in the top of the Xiaoerbulake Formation in the CT1 well block with a thickness of ~10 m and comprises dolostone and interbedded thin layers of oolitic dolostone and anhydrite-bearing dolostone (Figure 4F).

Interpretation: The occurrence of crystallization textures and crystallization fabrics in F2 (Figure 3E–H) has been extensively documented and is deemed to stem from dolomitization and recrystallization [33,44]. Anhydrite was created through gypsum dehydration when buried at depths below the reaction isotherm, provided that the fluids could escape from the dehydrating system [45]. This transformation could even occur at shallow depths

owing to increased heat flows related to the emplacement of local crustal magmatic bodies. The gypsum formation can be described by two processes: (a) under near-surface conditions, gypsum in the overlying evaporite strata was dissolved by fresh water, and Ca and S infiltrated into the dolostone pores, replacing dolostone with gypsum [46]; (b) under the hot and arid paleoclimate conditions, the seawater evaporated continuously, the salinity increased and the sulfate in the water gradually crystallized and precipitated to form gypsum [47]. The medium-bedded and thick-bedded dolostone with anhydrite suggests that F2 was likely deposited in a tidal flat environment, as reported by other researchers [6,33,36].

4.1.3. Dolobindstone (F3)

Description: F3 is gray to dark gray in color and mainly comprises dolomitized stromatolites (Figure 5A,B), with a thickness exceeding 10 m. It is found mostly in the ST1 well block of the Bachu Uplift and the upper part of the Xiaoerbulake Formation in the YH5 well block in the Tabei Uplift. The stromatolite has a bright and dark layer structure, exhibiting wavy lamination (Figure 5A) and even lamination (Figure 5C) under the microscope. Birdseyes are common in the stromatolite of the ST1 well block. The birdseyes of wavy stromatolite exhibit plate and stripe shapes, incompletely filled with dolosparite, with a length of tens of centimeters (Figure 5A). Birdseyes in even stromatolite present isolated, spotted and irregular voids filled with dolosparite. The void walls of birdseyes in stromatolite have a pectinate or agate ring edge and lack geopetal structure.

F3 is present in TFA7 and TFA8 (Table 2; Figure 4G,H). TFA7 is ~30 m thick and is only developed in the YH5 well block. The dolomitized stromatolite in TFA7 is 1.5–5.3 m thick, and the thin-bedded argillaceous dolostone is 1–2.5 m thick. Dolomitized stromatolite and argillaceous dolostone occur in thin interbedded layers. TFA8 mainly comprises dolomitized stromatolites with a thickness of 5–17 m and is found in the YH5, ST1 and K2 well blocks.

Interpretation: The origin of the birdseye structures in stromatolites may be described by two main genetic models: bubbles and dry shrinkage after organic matter decomposition [48]. Dolosparite in birdseyes developed because of recrystallization owing to dolomitization [49]. Stromatolites are laminated organosedimentary deposits that have accreted due to a benthic microbial community dominated by cyanobacteria after having trapped and bound detrital sediment and/or formed the locus of mineral precipitation [33,50]. Growth forms of stromatolites are deemed to be predominantly controlled by water depths and the degree of water turbulence [33,51]. Even stromatolites are common in supratidal and intertidal calm water environments, while wavy stromatolites are common in intertidal and shallow subtidal environments with relatively strong hydrodynamic conditions. Therefore, the dominance of wavy stromatolites and stratiform stromatolites with birdseyes indicates that F3 was deposited in the tidal flat environment under hot and arid climatic conditions [52].

4.1.4. Dolomudstone (F4)

Description: F4 is generally dark gray to black in color and thin- to medium-bedded (1.4–9 m thick). It mainly comprises dolomicrite and is found in the upper beds of the Xiaoerbulake Formation in the QT1–1 well block, the lower part of the Xiaoerbulake Formation in the ZH1 well block and the middle part of the Xiaoerbulake Formation in the F1 well block. Microscopically, F4 mainly contains black organic-rich or bituminous dolomitic mud and dolomite (Figure 5D) without sedimentary structures and grain structures. Some dolomite crystals are dolomitized or recrystallized to microspar.

F4 is mainly present in TFA9 (Table 2; Figure 4I). TFA9 consists of lower dolomicrite (F4), middle–lower argillaceous dolostone, upper crystalline dolostone and thin-bedded argillaceous dolostone. It is found in the middle–lower part of the Xiaoerbulake Formation of the F1 and ZH1 well blocks.

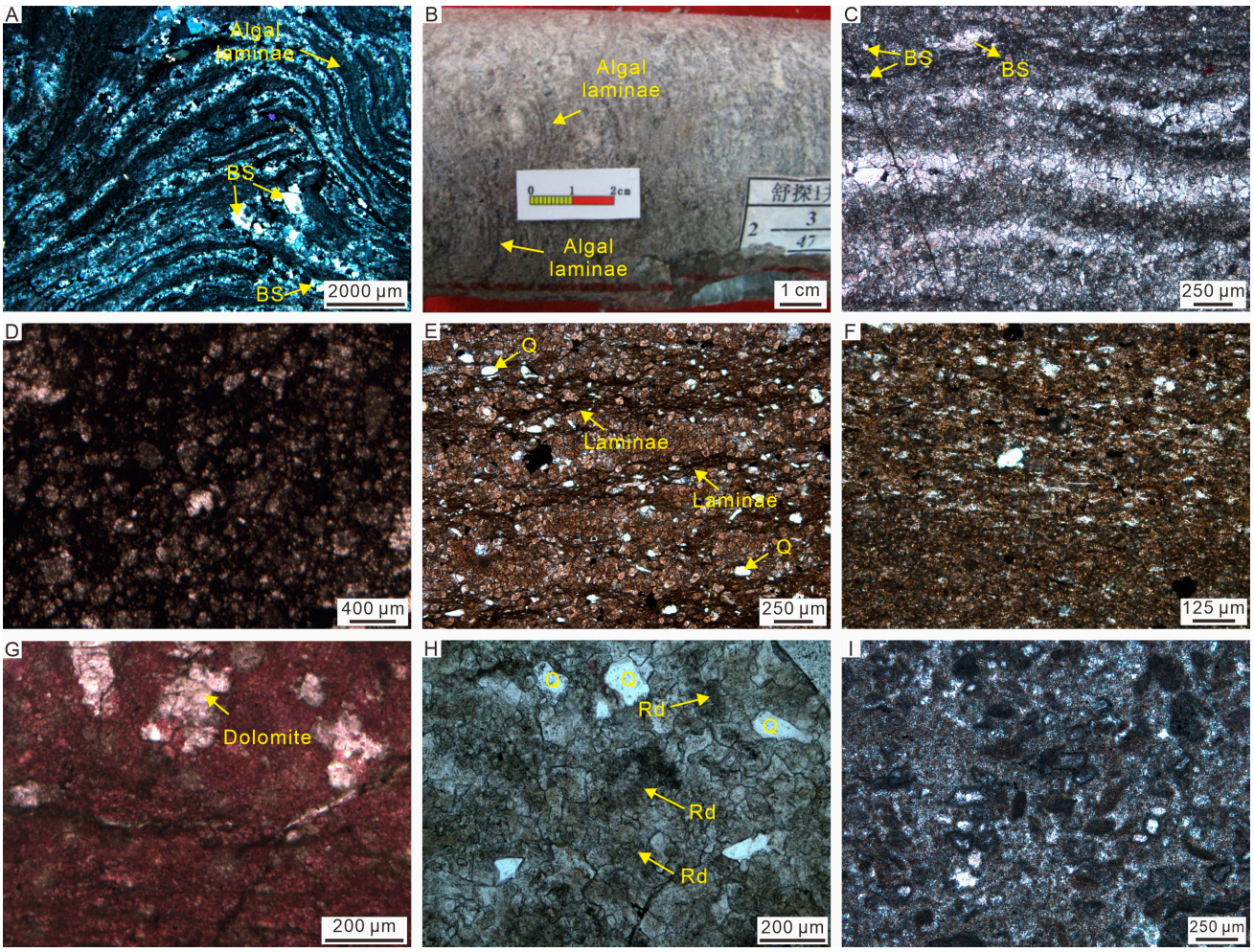


Figure 5. Photomicrographs and core images of FA1, FA2 and FA3 of the Early Cambrian Xiaoerbulake Formation in the Tarim Basin, Northwest China. (**A**) Wavy stromatolites with birdseyes, Well ST1, depth 1883.4 m. (**B**) Stromatolites, Well ST1, depth 1883.38 m. (**C**) Even stromatolites, Well ST1, 1886.22 m. (**D**) Dolomicrite, Well QT1–1, depth 5953 m. (**E**) Laminated argillaceous dolostone with silty quartz grains (Q), Well ST1, depth 1994.98 m. (**F**) Silt-bearing argillaceous dolomicrite, Well ST1, depth 1995.4 m. (**G**) Mud-bearing limestone, Well QT1–1, depth 5878 m. (**H**) Residual doloarenite (Rd) with fine-grained scattered quartz grains (Q), Well CT1, depth 7786 m. (**I**) Doloarenite, Well ST1, depth 2058.96 m. BS: birdseyes; Q: grain; Rd: residual doloarenite.

Interpretation: The absence of sedimentary and grain structures and the presence of black-colored dolomicrite in F4 suggest a protected lagoon marine setting with anoxic conditions [53].

4.1.5. Argillaceous Dolostone (F5)

Description: F5 is brown and dark gray in color and thin- to thick-bedded (0.8–10 m thick). It mainly comprises silt-bearing argillaceous dolostone (Figure 5E,F) and is found in the middle beds of the Xiaoerbulake Formation in the ZS1, F1 (Fang1) and ZS5 well blocks, in the lower part of the Xiaoerbulake Formation in the YH5 and ZH1 well blocks and in the upper part of the Xiaoerbulake Formation in the QT1–1 well block. Microscopically, F5 comprises silt-sized dolomite (Figure 5E) or mud-sized dolomite (Figure 5F), mud matrix and silty quartz grains with silty and argillaceous laminae. Crystallized textures of silt-sized dolomite are characterized by equigranular, tightly packed anhedral and subhedral crystals. Silty quartz grains are angular and scattered in the dolomite crystals and mud matrix (Figure 5E).

F5 is mainly present in TFA10 and TFA11 (Table 2; Figure 4J,K) and also observed in TFA5 and TFA7 (Figure 4E,G). TFA10 is ~40 m thick and is found in the upper part of the Xiaoerbulake Formation of the QT1–1 well block. In this type of facies association, F4 occurs as a thin interbedded layer in the upper part with a thickness of 3.7 m. TFA10 is ~25 m thick in the middle part of the Xiaoerbulake Formation in the ST1 well block and is up to 40 m thick in the middle–upper part of the Xiaoerbulake Formation in the QT1–1 well block. F5 is usually intercalated in limy dolostone, mud-bearing limestone (Figure 5G) and dolomicrite, as described in TFA10 and TFA11 (Figure 4J,K), and in dolostone and stromatolites, as described in TFA5 and TFA7 (Figure 4E,G).

Interpretation: The dominance of mud and the presence of scattered angular silty quartz grains with silty and argillaceous laminae point to a lower-energy depositional setting adjacent to the paleohighs [54]. The occurrence of silt-bearing argillaceous dolostone with silty and argillaceous laminae as interbedded thin layers in TFA5, TFA6 and TFA10 indicates that F5 was deposited in a low-energy, tidal flat environment [55] or restricted lagoonal environment [56].

4.1.6. Dolograinstone (F6)

Description: F6 comprises six lithotypes, sand-bearing dolarenite (Figure 5H), dolarenite (Figures 5I and 6A,B), oolitic dolopackstone (Figure 6C), oolitic dolograinstone (Figure 6D,E), thrombolites (Figure 6F) and algal lumpy dolograinstone (Figure 6G), which widely occur in the well blocks of the Bachu Uplift and the Tazzhong Uplift and in the KT1 well block, except for the oolitic dolopackstone. Sand-bearing dolarenite is gray in color with a bed thickness of ~9 m and is found at the base of the Xiaoerbulake Formation in the CT1 well block. Microscopically, fine-grained quartz grains are mainly angular and are scattered among grains of doloarenite, with amounts of 5%–10%. Dolarenite is brown-gray to gray in color and thin–thick-bedded (1.5–38 m thick). Microscopically, the residual texture of dolarenite is distinctly observed, and the grain size varies from 0.1 mm to 0.9 mm, with crystallized textures of inequigranular and anhedral crystals. Oolitic dolograinstone is yellowish white to gray in color and thin–medium-bedded (3–14 m thick). Microscopically, the ooids are 0.07–0.9 mm in diameter and are oval and spherical in shape. They are characterized by high concentrations, spheroidal and ellipsoidal shapes, and moderately to well-sorted and grain-supported texture with sparite dolomite cements. Dolomite crystals of ooids are equigranular, tightly packed anhedral, silt-sized and finely crystalline (Figure 6C,D). Although ooids' nuclei and concentric laminae are hardly observed (Figure 6D,E), some ooids exhibit traces of their concentric microstructure (Figure 6D). The ooids ranging from 0.05 mm to 0.12 mm in size are observed in the top of the Xiaoerbulake Formation in the CT1 well block with a thickness of ~2 m. According to the ooid structure and preservation, this lithotype can be classified into micrite, radial and recrystallized ooids (Figure 6C). Micrite ooids often occur together with radial ooids with anhydrite and silica (Figure 5B), displaying neither concentric nor radial microfabrics. Radial ooids vary from 0.08 mm to 0.12 mm in diameter. The radial–fibrous crystals build the inner part of the ooids and occur within the concentrically arranged outer laminae (cortices), with micritic fabric filling the ooid nuclei. Recrystallized ooids are 0.07–0.09 mm in size, and the crystal texture is characterized by a single dolomite crystal (Figure 6B). Thrombolites and algal lumps are usually observed in the same beds (Figure 6F,G). They are gray to dark gray in color and thin- to thick-bedded (from 1.5 m to more than 100 m thick). Under the microscope, clots and lumps exhibit irregular (Figure 4I), broken lobate (Figure 6F) and oval shapes (Figure 6G), with sizes of 0.15–1.5 mm. The components among them are silt-sized and finely crystalline dolosparites, and calcite found in low concentrations.

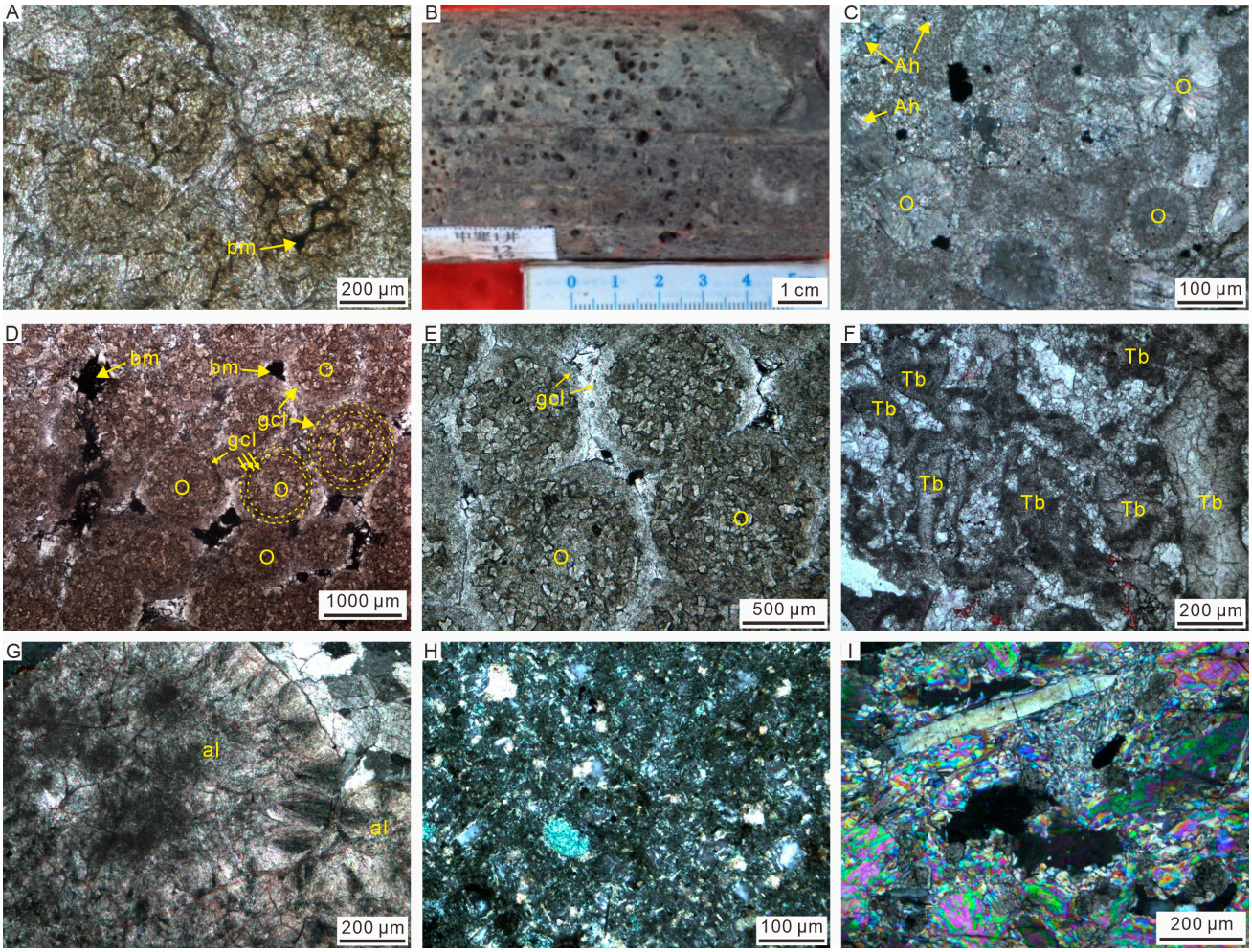


Figure 6. Photomicrographs and core images of FA3, intrusive rock and FA4 of the Early Cambrian Xiaoerbulake Formation in the Tarim Basin, Northwest China. (**A**) Doloarenite, Well ZS1, depth 6766 m. (**B**) Doloarenite with vuggy pores, Well ZH1, depth 7408.1 m. (**C**) Oolite with anhydrite, Well CT1, depth 7728 m. (**D**) Dolomitized ooids showing ghosts of concentric laminae and intergranular pores filled with bitumen (bm), Well CT1, depth 7767.93 m. (**E**) Ooids with complete replacement dolomitization, Well CT1, depth 7766.67 m. (**F**) Thrombolites, Well KT1, depth 4830 m. (**G**) Algal lump (al), Well KT1, depth 4835 m. (**H**) Diabase, Well KT1, depth 4820 m. (**I**) Anhydrite–salt rock, Well K2, depth 5548 m. gcl: ghosts of concentric laminae; bm: bitumen; Ah: anhydrite; Q: grain; Tb: thrombolite; O: ooid; al: algal lump.

F6 is mainly present in TFA12–17 (Table 2; Figure 7A–F). TFA12 comprises sand-bearing dolarenite, an interbedded thin layer of dolostone and oolitic dolostone from base to top (Figure 7A). It has a thickness of up to 30 m and occurs in the lower part of the Xiaoerbulake Formation in the CT1 well block. TFA13 demonstrates a vertical stacking pattern of dolarenite, oolitic dolostone and dolostone interlayers (Figure 7B), with a thickness of 20–60 m. It is mainly developed in the middle–upper part of the Xiaoerbulake Formation in the ZH1 well block and in the upper part of the Xiaoerbulake Formation in the H4 and CT1 well blocks. TFA14 consists of thrombolites and algal lumps (Figure 7C), with a thickness of 17–70 m, and is mainly found in the lower part of the Xiaoerbulake Formation in the ST1 and KT1 well blocks. TFA15 is ~40 m thick and mainly distributed in the upper part of the Xiaoerbulake Formation in the F1 well block. It is made up of dolarenite (30 m thick) and interbedded thin layers of algal dolostone (2–4 m thick) (Figure 7D). TFA16 is characterized by a vertical superposition of dolarenite and oolite with thin-bedded algal dolostone (Figure 7E). It is mainly found in the upper part of the Xiaoerbulake Formation in

the CT1 well block with a thickness of ~20 m. TFA17 comprises oolitic, dolarenite and algal dolostone superimposed vertically (Figure 7F). It is mainly developed in the middle–lower part of the Xiaoerbulake Formation in the K2 well block, with a thickness of ~40 m. The overlying formation is anhydrite rock of the Wusonggeer Formation, while the underlying formation is TFA16.

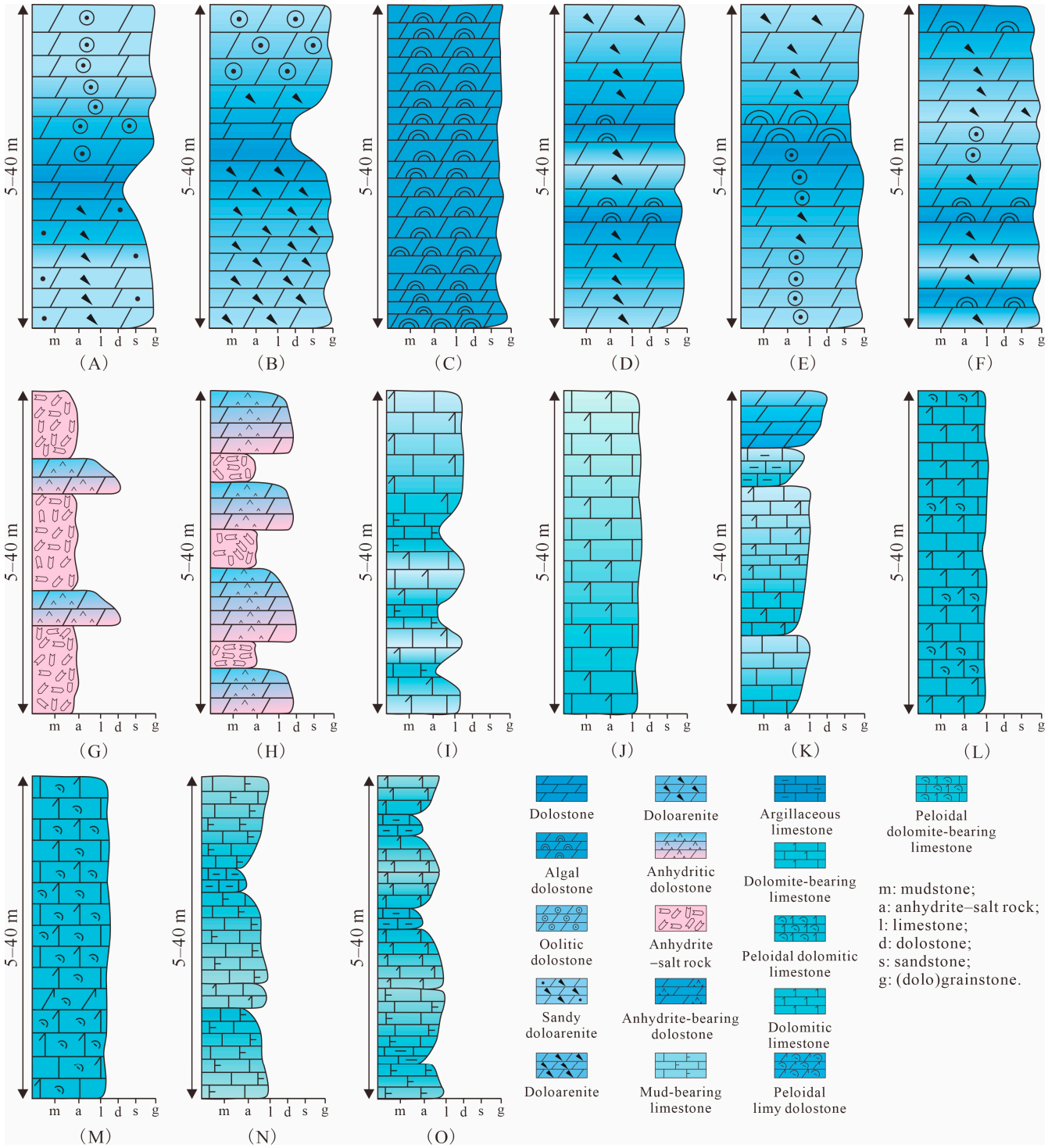


Figure 7. TFA12–26 of FA3–7 of the Early Cambrian Xiaoerbulake Formation in the Tarim Basin, Northwest China. (**A**) TFA12; (**B**) TFA13; (**C**) TFA14; (**D**) TFA15; (**E**) TFA16; (**F**) TFA17; (**G**) TFA18; (**H**) TFA19; (**I**) TFA20; (**J**) TFA21; (**K**) TFA22; (**L**) TFA23; (**M**) TFA24; (**N**) TFA25; (**O**) TFA26.

Interpretation: The angular shape of the quartz grains possibly suggests that the grains were transported to the carbonate ramp by rivers and currents for a short distance [57] or their transport was related to wind blowing [42,58]. The absence of ooid nuclei and some ghost features of concentric laminae imply the destruction of original structures [59]. Micritic fabric and silt-sized to sand-sized dolomite grains commonly filling ooid cortices, concentric laminae and nuclei are likely the result of diagenetic alteration (burial dolomitization) of primary minerals [59,60], which started with an initial precipitation along the grain periphery and was subsequently followed by dolomite precipitation along the porous cortical laminae [33,61]. The common presence of varied medium to coarse sand-sized grainstones and the vertical superpositions of oolites with high amounts of ooids, dolarenite, thrombolites and algal lumps indicate that F6 was deposited in a high-energy shoal environment [33,42,54,56,62]. Notably, the presence of all the ooids is not indicative of a high-energy sedimentary environment. Well-sorted and fine sand-sized oolites with micrite, radial and recrystallized ooids (Figure 8B) were likely formed in a relatively calm or low-energy lagoon. Alternatively, they were perhaps reworked and transported into a low-energy setting [33,63].

4.1.7. Anhydrite–Salt Rock (F7)

Description: F7 is light brown to brown in color and thin–medium-bedded (1.5–7 m thick). Under the microscope, the evaporite mainly comprises anhydrite and a small amount of dolostone (Figure 3H). The anhydrite crystals exhibit a lath-like shape, and their concentration exceeds 90%, while the dolostone concentration is <10% (Figure 6I).

F7 is present in TFA18 and TFA19 (Table 2; Figure 7G,H). TFA18 comprises anhydrite–salt rock and thin–medium interlayers of anhydritic dolostone and is found in the middle part and top of the Xiaoerbulake Formation in the K2 well block, with a thickness of ~40 m. The underlying and overlying stratum are TFA7 and TFA4, respectively. TFA19 is 8–24 m thick and composed of anhydritic dolostone and interbedded thin layers of anhydrite–salt rock. It mainly occurs in the upper part of the Xiaoerbulake Formation in the K2 well block and in the lower–middle part of the Xiaoerbulake Formation in the H4 well block. The underlying and overlying stratum of TFA19 is TFA4.

Interpretation: The anhydrite developed from the initial gypsum crystals that had grown and later dehydrated to form anhydrite in the buried environment [6,64]. The dominant occurrence of anhydrite in F7 points to a hot and arid, hypersaline sabkha setting, similar to that of the modern gypsum deposits along the western coast of the Persian Gulf [64].

4.1.8. Microcrystalline Limestone (F8)

Description: F8 is gray to dark gray in color and medium- to thick-bedded (18 m to over 100 m thick). It comprises dolomite-bearing and dolomitic microcrystalline (microsparitic) limestone. Microscopically, it is mainly made up of calcite, dolomite, bioclast and a small amount of pyrite (Figure 8A,B). Calcite was completely recrystallized and partially dolomitized. Calcite and dolomite are characterized by microspar textures, with crystal sizes < 0.03 mm in diameter. Wavy and horizontal laminae are locally observed.

F8 is extensively distributed in the Xiaoerbulake Formation in the Tabei Uplift and XSC1 well blocks and is present in TFA20–22 (Table 2; Figure 7I–K). TFA20 occurs within the Xiaoerbulake Formation in the QT1–2, XSC1 and LT3 well blocks; TFA21 is found in the Xiaoerbulake Formation in the QT1–2, XSC1 and LT3 well blocks and TFA22 is mainly developed in the top of the Xiaoerbulake Formation in the QT1–2 well block. TFA20, TFA21 and TFA22 coexist with F9 and F10 (Figure 7I,K,L,N,O).

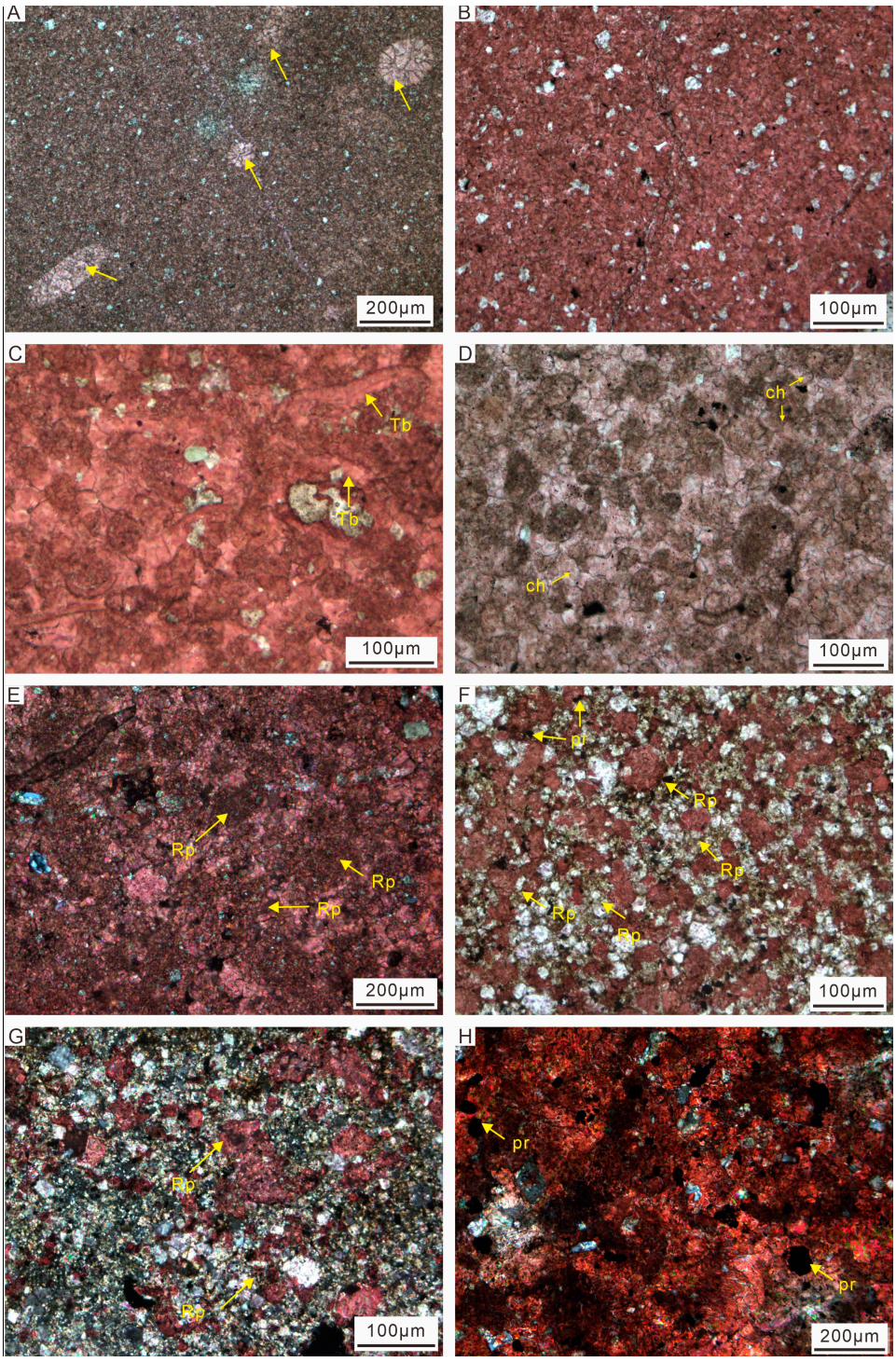


Figure 8. Photomicrographs of FA5, FA6 and FA7 of the Early Cambrian Xiaoerbulake Formation in the Tarim Basin, Northwest China. (**A**) Dolomitic limestone with bioclastics (arrows), Well XH1, depth 7510 m. (**B**) Dolomite-bearing limestone, Well LT1, depth 8400 m. (**C**) Peloidal dolomite-bearing limestone with trilobites, Well LT1, depth 8560 m. (**D**) Peloidal dolomite-bearing limestone with calthrops, Well LT3, depth 8369.01 m. (**E**) Peloidal dolomite-bearing limestone, Well XH1, depth 7565 m. (**F**) Peloidal dolomitic limestone with residual peloids and pyrite, Well LT3, depth 8365.38 m. (**G**) Peloidal limy dolostone, Well LT3, depth 8362.10 m. (**H**) Argillaceous limestone with a small amount of silicated dolostone and pyrite, Well LT3, depth 8495 m. Tb: trilobite; bm: bitumen; ch: calthrop; Rp: residual peloid; pr: pyrite.

Interpretation: Microspar limestone likely originated from lime mudstone or silt-sized carbonate grains (peloidal grainstone) [65]. The original textures of the grains were destroyed due to strong recrystallization during the diagenetic process. The presence of medium- to thick-bedded microcrystalline limestone with trilobite bioclasts and the vertical stratal relationship with F8 and F10 indicate that F9 was deposited in an inter-shoal environment of the mid-ramp [66].

4.1.9. Peloidal Grainstone (F9)

Description: Three lithotypes are recognized in F9 according to the dolomite and calcite concentrations. These are peloidal dolomite-bearing limestone (Figure 8C–E), peloidal dolomitic limestone (Figure 8F) and peloidal limy dolostone (Figure 8G). Dolomite-bearing limestone is gray to dark gray in color and commonly occurs in the Xiaoerbulake Formation of the Tabei Uplift, with a thickness ranging from 5 m to 80 m. Microscopically, it is dominated by a large amount of small (from 0.03 mm to 0.2 mm in size), poorly to moderately sorted, subrounded and subangular peloids with trilobite and monaxon fragments. Peloids comprise mud-sized and very finely crystalline calcites and have no internal structures. They are cemented by very finely crystalline calcite and small amounts of very finely crystalline dolomite. Peloidal dolomitic limestone and peloidal limy dolostone are gray in color. Peloidal dolomitic limestone is found in the upper part of the Xiaoerbulake Formation in the XH1 well block and in the top of the Xiaoerbulake Formation in the LT3 well block with a thickness of 4–10 m. Peloidal limy dolostone is only observed in the top of the Xiaoerbulake Formation in the LT3 well block with a thickness of 3.5 m. Though these two lithotypes were extensively dolomitized, a respectable amount of calcitized peloids have preserved grain structure and can be distinguished from dolomite. Microscopically, the peloid components also comprise very finely crystalline calcite as dolomite-bearing peloidal limestone is embedded in recrystallized dolomite. The dolomite crystals exhibit very fine, inequigranular and anhedral to euhedral crystallization textures.

F9 is present in TFA23 and TFA24 (Table 2; Figure 7L,M). TFA23 comprises dolomitic limestone (with a dolomite content of 25%–50%) or dolomite-bearing limestone (with a dolomite content of 5%–25%) interbedded with dolomite-bearing peloidal limestone and is found in the middle–upper part of the Xiaoerbulake Formation in the XH1 well block and in the top and lower parts of the Xiaoerbulake Formation in the LT1 well block. TFA24 comprises medium–thick-bedded peloidal dolomite-bearing limestone and peloidal dolomitic limestone interbedded with a thin layer of peloidal limy dolostone vertically and is found in the lower part of the Xiaoerbulake Formation in the LT1 well block and in the top of the Xiaoerbulake Formation in the LT3 well block.

Interpretation: The presented characteristics of peloids in F9 indicate that these grains likely resulted from the reworking of weakly lithified carbonate mud located in F8 by storm waves [33,67]. Subsequently, the peloids were recrystallized from micrite-sized calcite crystals during recrystallization. The dominance of peloids in F9, the absence of coarse amalgamated tempestites in F9 and the overlying and underlying strata and the vertical stratal relationship with F8 and F10 demonstrate that unlike F6, F9 was deposited in a relatively low-energy shoal environment of the mid-ramp [1,33,68].

4.1.10. Argillaceous Limestone (F10)

Description: F10 is dark gray in color and thin–thick-bedded (2–8 m thick). Under the microscope, it mainly comprises calcite, terrigenous mud and a small amount of dolomite (Figure 8H). Calcite was completely micritized and locally dolomitized. Calcite and dolomite are characterized by very fine crystalline textures, with crystal size < 0.025 mm. Terrigenous mud was infected with organic matter and bitumen.

F10 usually occurs in thin interbedded layers between mud-bearing, very finely crystalline dolomitic limestone, very finely crystalline dolomitic limestone and very finely crystalline limestone. It is present in TFA25 and TFA26 (Table 2; Figure 7N,O). TFA25 is found in the middle–lower part of the Xiaoerbulake Formation in the QT1–2 and LT3 well

blocks, while TFA26 is distributed in the lower part of the Xiaoerbulake Formation in the XH1 well blocks. Vertically, TFA25 and TFA26 lie over black shale or black siliceous shale of the Wusonggeer Formation in the LT3, LT1, QT1–2 and XH1 well blocks in the Tabei Uplift.

Interpretation: The presence of black terrigenous mud and the vertical stratal relationship with black shale or black siliceous shale of a deep outer ramp in the Wusonggeer Formation indicate that F10 was deposited in a deeper water environment, mostly a shallow outer ramp [1,33,69]. The noncarbonate concentrations of terrigenous mud increase as the deposition rate decreases near the far terrigenous end of a mixed siliciclastic–carbonate ramp [69], suggesting a deeper water environment.

4.2. The Distribution of Facies Associations

To better clarify the lateral distribution and spatial evolution of the facies associations of the Xiaoerbulake Formation, we selected two well-based correlation sections oriented NW–SN and EW for systematic analysis (Figures 9 and 10). The interwell facies characteristics of well-based correlation sections mainly follow the work on the sedimentary facies and lithofacies paleogeography of the Xiaoerbulake Formation reported by other researchers [12,14,19,25,28,70]. From the KT1 well block to the ZH1 well block in the Tazhong Uplift, the depositional environment is an inner ramp. The sedimentary thickness gradually decreases, reflecting the affection of the Southwestern Tarim Uplift. In the direction of the Southwestern Tarim Uplift (from the KT1 and ZH1 well blocks to the CT1 well block), the lower part of the Xiaoerbulake Formation is represented by the high-energy shoal facies association. The sedimentary thickness gradually thins and the depositional environment grades into a tidal flat facies association in the H4 well block. The middle part of the Xiaoerbulake Formation is dominated by the lagoon facies association, which is mutated into the sabkha facies association in the H4 well block and is not present in the CT1 well block. The upper part of the Xiaoerbulake Formation is mainly characterized by the high-energy shoal facies association or tidal flat facies association to high-energy shoal facies association. In the region near the Southwestern Tarim Uplift, oolitic shoals and sand-size grain shoals are commonly observed in the high-energy shoal facies association (Figure 9). From the K2 well block in the Bachu Uplift to the LT3 well block in the Tabei Uplift, the sedimentary thickness of the Xiaoerbulake Formation tends to increase, evolving from 195.7 m in Well K2 to 363 m in Well LT1. The depositional environment changes from the inner ramp to the middle ramp and subsequently to the outer ramp. The facies associations evolve from the vertical stacking combination of FA3, FA4 and FA1 and the vertical stacking combination of FA3, FA1, FA2 and FA3 in the K2 and F1 well blocks in the Bachu Uplift to the vertical stacking combination of FA7, FA6 and FA5 in the XH1 and LT1 well blocks and subsequently to FA7 in the LT3 well block (Figure 10).

4.3. Depositional Model

From the facies associations of the Early Cambrian Xiaoerbulake Formation in the Tarim Basin, a depositional model of a carbonate ramp from paleohighs to depressions has been noted (Figure 11). The carbonate ramp in the Xiaoerbulake Formation comprises an inner ramp, a middle ramp and an outer ramp environment. Of these, the inner ramp includes a tidal flat facies association, a lagoon facies association, a sabkha facies association and a high-energy shoal facies association; the middle ramp includes an inter-shoal sea facies association and a low-energy shoal facies association and the outer ramp mainly comprises an open-shelf facies association (Table 2). Jointly controlled by the paleogeographic framework with three paleohighs (Wuqia Paleohigh, Southern Tarim Paleohigh and Keping–Wensu Paleohigh) and two depressions (Southwestern Tarim Depression and North Depression) during the sedimentary period of the Xiaoerbulake Formation [12,14,25,28], the carbonate ramp deposits demonstrate the difference between the depositional environments, facies associations and facies types in different regions of the Tarim Basin. The depositional environment was an inner ramp, a middle ramp and an outer ramp from the Wuqia Paleohigh in the western Tarim Basin to the eastern deep-water basin (Figure 11). The inner ramp occurs

above the fair weather wave base and is typically found in the Bachu Uplift, Tazhong Uplift and KT1 well block. Affected by terrigenous inputs, a set of mixed siliciclastic–carbonate rocks of a tidal flat facies association was mainly deposited adjoining the paleohighs. It graded into crystalline dolostone and bindstone of a tidal flat facies association or sabkha facies association, lagoon facies association and high-energy shoal facies association toward the depressions. The middle ramp is located between the fair weather wave base and the storm wave base and is mainly distributed in the middle of the Tabei Uplift, Bachu Uplift and Tazhong Uplift. It is sequentially composed of microcrystalline limestone of inter-shoal facies association and peloidal grainstone of low-energy shoal facies association toward the depressions (Southwestern Tarim Depression and North Depression). The outer ramp occurs in the depositional environment below the normal storm wave base. The seawater in the depositional area is calmer than that of the middle ramp. The distribution position is roughly similar to that of the middle ramp on the plane and different in space. It mainly comprises the open-shelf facies association.

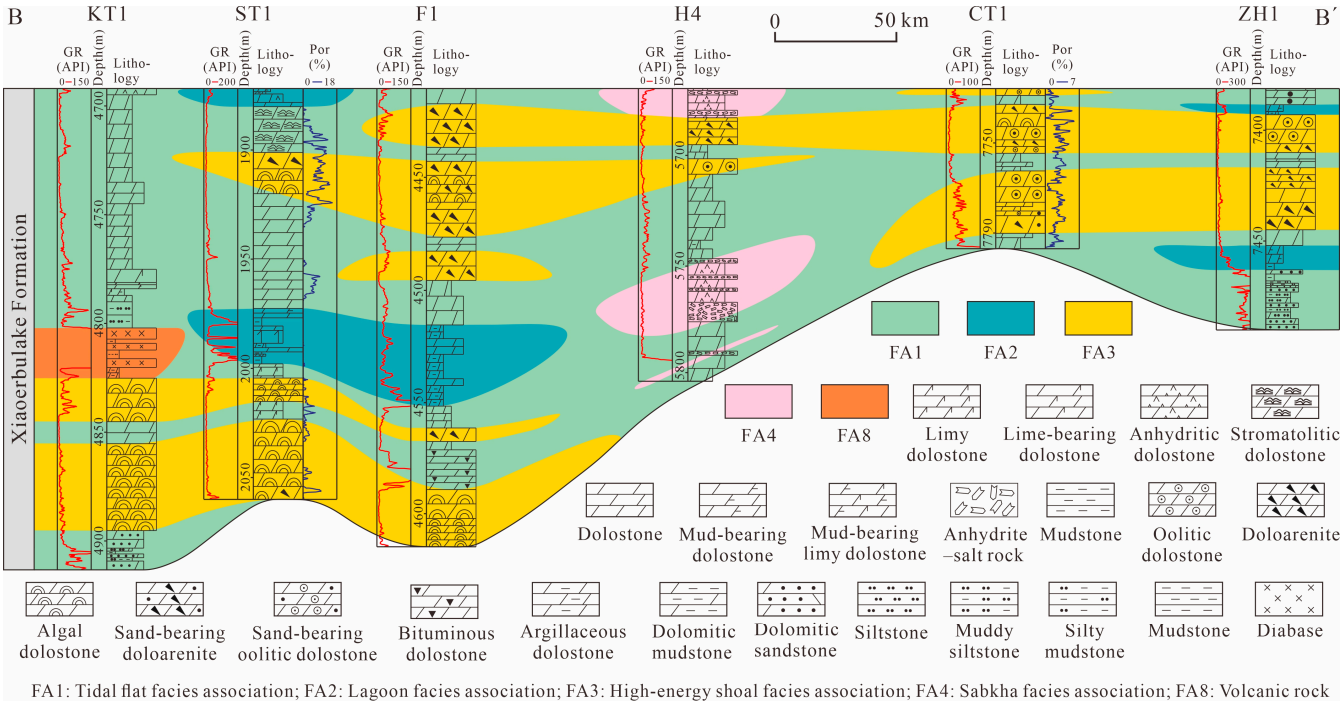


Figure 9. Well-based facies association distribution in the NW–SE direction (KP1 well block–Bachu Uplift–Tazhong Uplift) of the Early Cambrian Xiaoerbulake Formation in the Tarim Basin (the location of cross-well profile B–B′ is shown in Figure 1). Por: porosity, the porosity data from well logging interpretation. B: the starting location of the cross-well profile (B–B′); B′: the end location of the cross-well profile (B–B′).

4.4. Reservoir Pore Systems

According to the microscopic characteristics of thin sections, five main pore types are identified: interparticle pores, intraparticle pores, intercrystalline pores, vuggy pores and moldic pores (Figure 12).

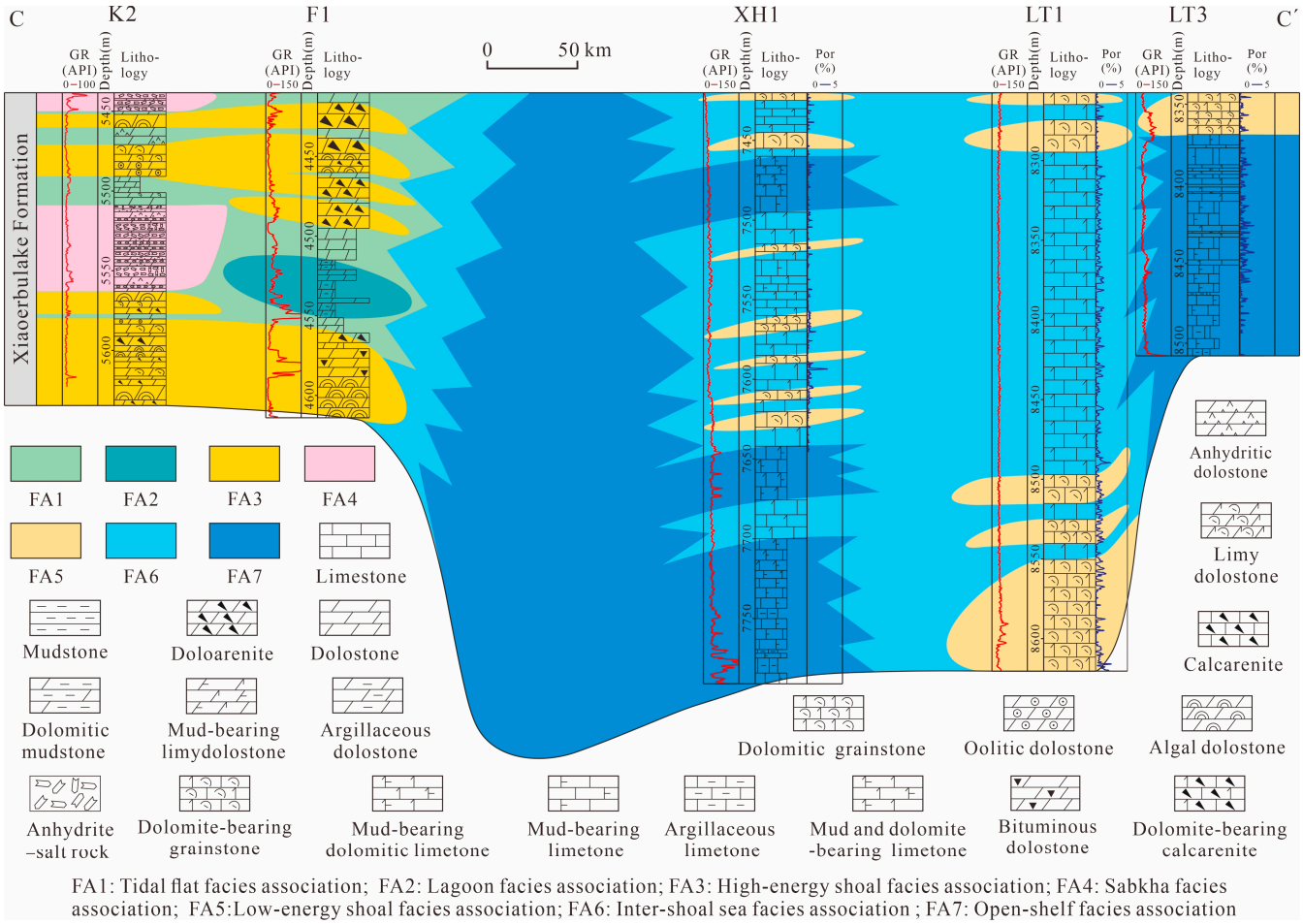


Figure 10. Well-based facies association distribution in EW direction of the Early Cambrian Xiaoerbulake Formation in the Tarim Basin (the location of cross-well profile C–C′ is shown in Figure 1). Por: porosity; the porosity data from well logging interpretation. C: the starting location of the cross-well profile (C–C′); C′: the end location of the cross-well profile (C–C′).

4.4.1. Interparticle Pores

The term "interparticle pore" presented herein is used to describe the pores formed between grains (intergrain), which agrees with the definition provided by [71]. Interparticle pores primarily occur in dolograinstone of high-energy shoal facies association, including sand-bearing dolarenite, dolarenite and oolitic dolostone. The pores occur between ooids and sand-sized grains, mostly exhibiting irregular polygonal and embayed shapes. These pores are filled with bitumen, anhydrite cements and coarsely crystalline dolomite (Figure 12A–C). Dolomite cements exhibit clear crystal faces and euhedral and subhedral crystal shapes. This pore type is characterized by large pore sizes ranging from 0.03 mm to 1 mm, while some solution-enlarged interparticle pores are up to 2 mm in diameter. Interparticle pores are commonly related to the selective dissolution of cements and matrix, strongly controlled by fluid migration pathways and the patchy cementation of both primary and secondary interparticle pores [72].

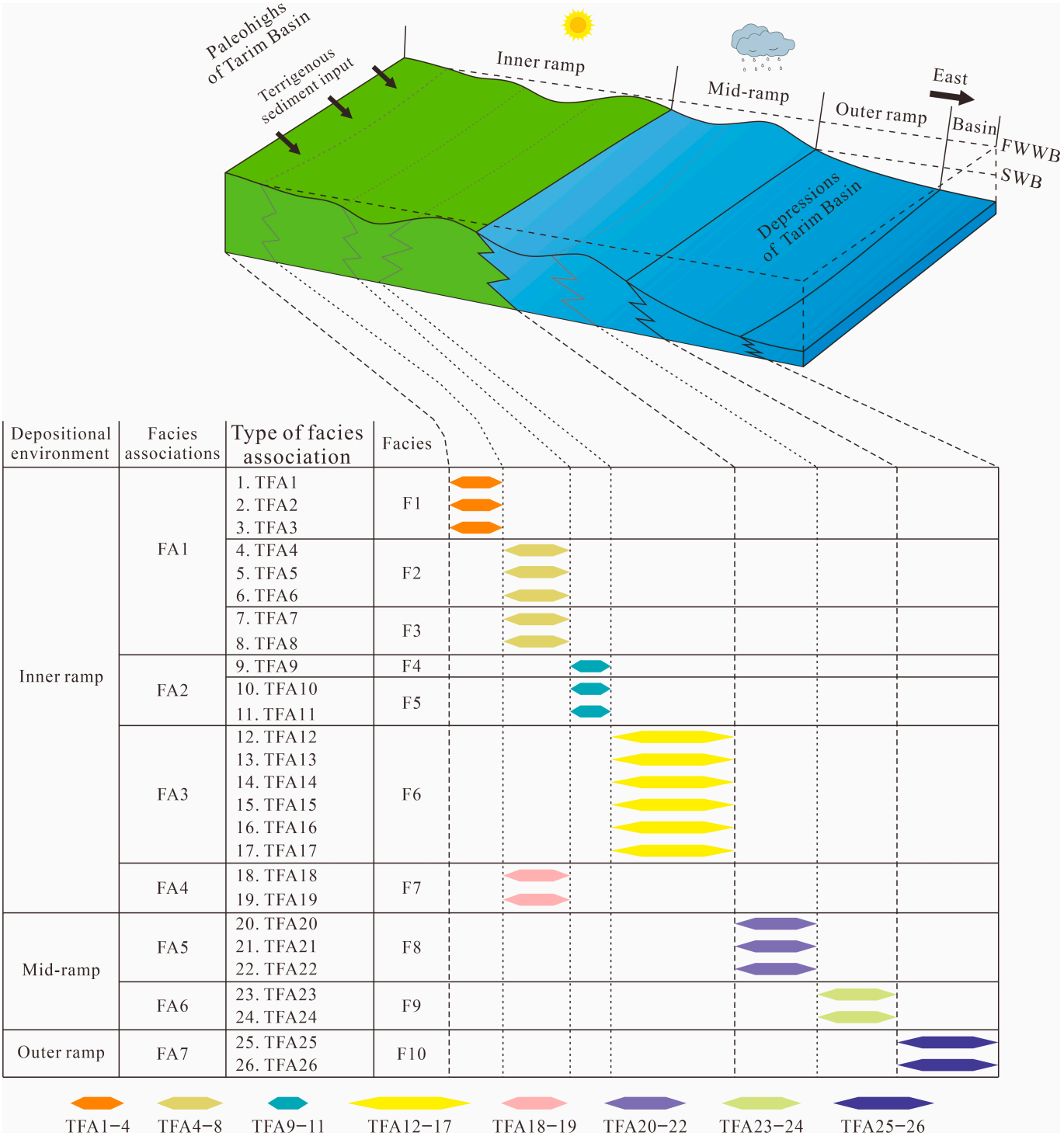


Figure 11. Schematic depositional model of the Early Cambrian Xiaoerbulake Formation in the Tarim Basin showing distribution patterns of the facies and facies associations developed in different parts of an Early Cambrian carbonate ramp.

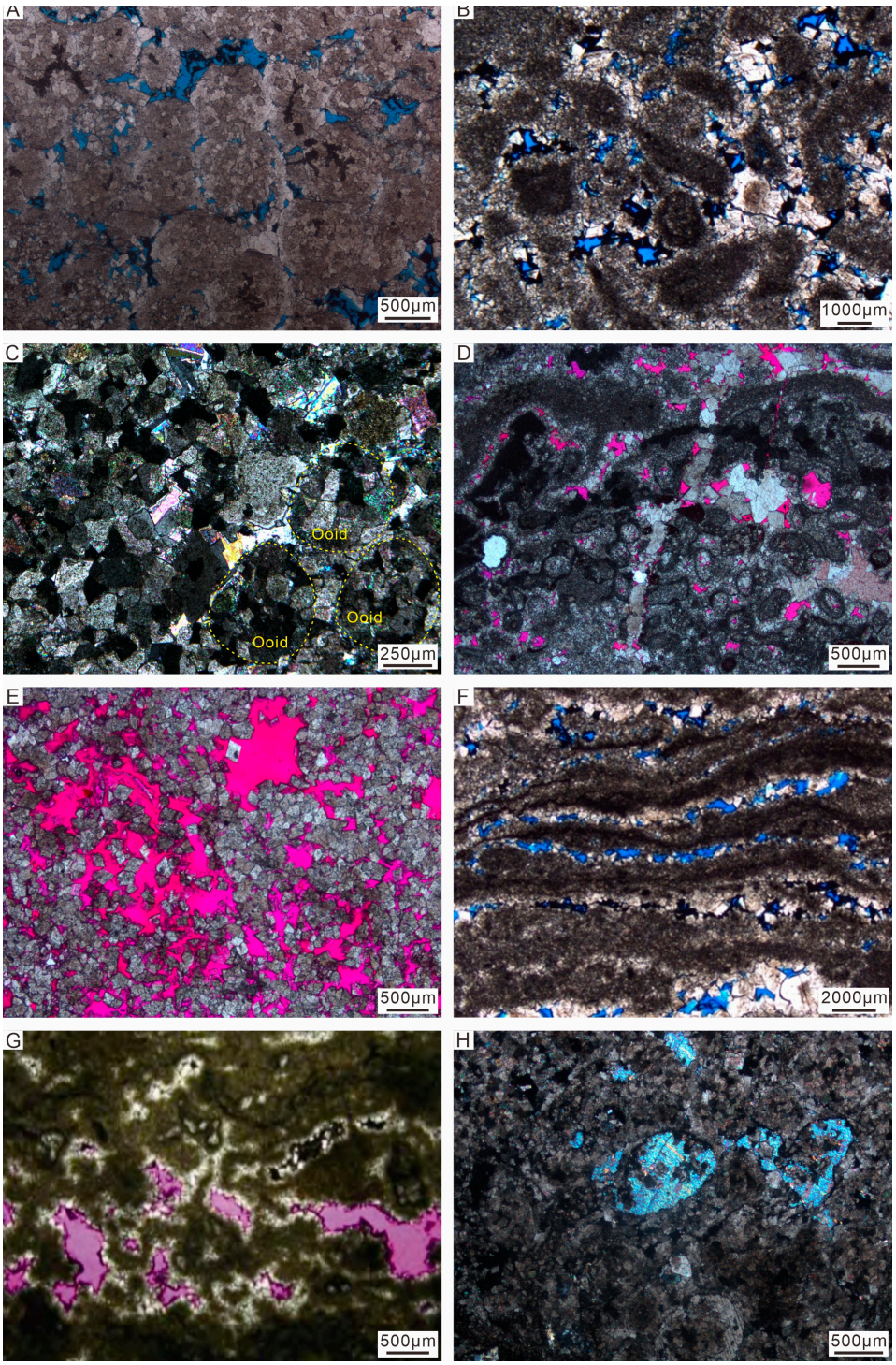


Figure 12. Types of reservoirs and pores of the Early Cambrian Xiaoerbulake Formation in the Tarim Basin. (**A**) Interparticle pores and intraparticle pores of oolitic dolostone, Well CT1, depth 7767.93 m. (**B**) Interparticle pores and intraparticle pores of doloarenite, Well ST1, depth 1886 m. (**C**) Interparticle pores and intraparticle pores of oolitic dolostone filled with anhydrite, Well CT1, depth 7764.99 m. (**D**) Interparticle pores and intraparticle pores of algal doloarenite, Well ST1, depth 1883.07 m. (**E**) Intercrystalline pores and vuggy pores of finely crystalline dolostone, Well ST1, depth 1915.75 m. (**F**) Vuggy pores of stromatolite, Well ST1, depth 1885.6 m. (**G**) Vuggy pores of algal dolostone, Well F1, depth 4599 m. (**H**) Moldic pores of oolitic dolostone completely filled with anhydrite, Well CT1, depth 7764.24 m.

4.4.2. Intraparticle Pores

Intraparticle pores are pore spaces occurring within sand-sized carbonate grains and ooids of the high-energy shoal facies association (Figure 12A,B,D). They form from the selective dissolution of interparticle cements, with sizes ranging from 0.01 to 0.35 mm. These pores are locally filled with anhydrite, suggesting that they likely formed during early dolomitization [73].

4.4.3. Intercrystalline Pores

Various levels of intercrystalline pores are observed under the microscope in the finely to medium crystalline dolomite owing to various degrees of dolomitization [74]. In the studied dataset, intercrystalline pores are developed between euhedral dolomite crystals (Figure 12E). Additionally, in some cases, intercrystalline pores are enlarged by dissolution along the boundaries, creating intercrystalline dissolved pores with irregularly banded and embayed shapes. The sizes of intercrystalline pores range from 0.01 mm to 0.3 mm. These intercrystalline pores occur in finely crystalline dolostone of the high-energy shoal facies association with residual grain texture (Figure 12E).

4.4.4. Vuggy Pores

Vuggy pores are secondary solution pores formed by the dissolution of cement, matrix and grains [71]. They are affected by near-surface meteoric waters and are related to deep burial fluids, mainly controlled by fractures and faults [72,75]. Herein, vugs occur as algal framework dissolution pores and irregular solution-enlarged intercrystalline pores (Figures 3A, 6B and 12E) and interparticle pores (Figure 12A,C,E,F) of the high-energy shoal facies association, with a pore size of 0.2–25 mm.

4.4.5. Moldic Pores

Moldic pores are secondary pores formed by the selective, complete or partial dissolution and recrystallization of grains or crystals [71,72]. Herein, they are commonly associated with partially or completely dissolved and recrystallized ooids and sand-sized grains (Figure 12D, E and H) of the high-energy shoal facies association, with pore sizes of 0.3–0.7 mm. In anhydrite-bearing oolitic dolostone, moldic pores within ooids are generally filled with anhydrite (Figure 12H).

5. Discussion

5.1. Controlling Factors in the Development of Facies and Facies Associations

At the depositional stage of the Xiaoerbulake Formation, in addition to the macro morphologic characteristics of "higher in the south and lower in the north", the basin also exhibited the macro morphologic characteristics of "higher in the west and lower in the east" [14,25,28,76]. Controlled by the continuous subsidence of the Luonan–Yubei Rift, the central basement paleohigh evolved into the Wuqia and Tanan (Southern Tarim) Paleohighs [77]. The original Tabei (northern Tarim) basement paleohigh maintained the pattern of near-EW trend and higher west and lower east during the early period of the Early Cambrian. The Keping–Wensu region was a low paleohigh, while the Lunnan region was an underwater low paleohigh [78]. The Wuqia, Southern Tarim and Keping–Wensu Paleohighs together with the Southwest Tarim Depression and North Depression constituted a new paleogeographic pattern of "three paleohighs and two depressions" [79]. This structural pattern controlled the sedimentary thickness, depositional environment and facies associations of the Early Cambrian Xiaoerbulake Formation. The Xiaoerbulake Formation overlapped with the marginal region of the paleohighs and developed a set of carbonate ramp deposits [25]. From the periphery of the paleohighs to the depressions, the sedimentary thickness gradually increased from 38 m to372 m (Table 1). The depositional environments and facies associations successively developed from FA1 (F1, F2 or F3), FA2 or FA3 of the inner ramp to FA5 and FA6 of the middle ramp and FA7 of the outer ramp (Table 2).

Sea level changes and the paleoclimate also controlled the development of the Xiaoerbulake Formation. The sediments of the Early Cambrian Xiaoerbulake Formation were deposited during a transgression and a regression, the climate was arid and hot and the seawater salinity was relatively higher [21,80]. The relative sea level experienced a rise in the early sedimentary periods of the Xiaoerbulake Formation and subsequently dropped in the middle and late sedimentary period of the Xiaoerbulake Formation [81]. In the Bachu and Tazhong Uplifts, the facies associations evolved from a high-energy shoal facies association or a tidal flat facies association to a lagoonal facies association and subsequently to a high-energy shoal facies association or a tidal flat facies association, represented by Wells ST1, F1 and ZH1. The Xiaoerbulake Formation near the Southwest Depression and North Depression evolved from an open-shelf facies association of the outer ramp to an inter-shoal facies association or a low-energy shoal facies association of the middle ramp from the bottom to the top, represented by Wells LT1, QT1–2 and LT3 (Figures 1A, 9 and 10). During the middle and late stages of the deposition of the Xiaoerbulake Formation, affected by the arid paleoclimate, the salinity of the seawater increased and the anhydrite–salt rock gradually crystallized. The sabkha facies association occurred during the middle stage of the Xiaoerbulake Formation in some well blocks, represented by Wells K2 and H4. Birdseyes of different shapes can be observed in stromatolite (Figure 4A), represented by Wells ST1, CT1 and H4.

5.2. The Relationship between Facies Associations and Reservoir Quality

Facies associations and facies control the primary pore structure of the reservoirs and affect the preservation and transformation of pores [66,82]. High-energy shoal facies associations are usually located in the upwarped areas in a ramp. With a slow decline in the sea level, the sedimentary formations of high-energy shoal facies associations were gradually exposed and prone to freshwater leaching, dissolution and dolomitization, forming a dolomitized reservoir with residual particle texture and dissolution pores. The satisfactory compaction resistance of dolomite during this period preserved the original pores. During the burial stage, dissolution played an important role in reconstructing the early reservoirs, and the reconstruction intensity mainly depended on the physical properties of the early reservoirs. Currently, the reservoir pore space is mostly made up by the solution-enlarged pores [14].

In the studied dataset, the inner ramp high-energy shoal facies association exhibits good reservoir quality. Many reservoir pores, including interparticle, intraparticle, intercrystalline, vuggy and moldic pores, are observed in thin sections in the upper part of the Xiaoerbulake Formation. The porosity in Well ST1 (1879–1920 m) ranges from 1.4% to 7.5%, with an average porosity value of 4% [14], and the porosity in the 7726–7792 m of Well CT1 ranges from 2.9% to 4.8%, with an average porosity value of 3.65%. The mid-ramp and outer ramp depositional environments show poor reservoir quality. The porosity from well logging interpretation is lower than 2% (Figures 9 and 10).

5.3. Diagenetic Controls of Reservoir Quality

Because dolomitization and anhydrite cementation commonly exert a considerable impact on carbonate reservoir quality, they are major diagenetic processes investigated in carbonate hydrocarbon reservoir rocks [53,83,84].

5.3.1. Effects of Dolomitization

Dolomitization is one of the most important diagenetic processes in the Early Cambrian Xiaoerbulake Formation [28,70,73,83,85]. Multiple geochemical parameters show that the Early Cambrian Xiaoerbulake dolomite is mainly the product of sabkha evaporation dolomitization in a penecontemporaneous environment and seepage–reflux dolomitization in a shallow burial environment. Only a small amount of finely–medium crystalline dolomite was formed in an intermediate and deep burial environment [21,70]. Rapid dolomitization in a penecontemporaneous and shallow burial environment formed fine

dolomite crystals with a well-preserved fabric. Consequently, the dolostone in the Early Cambrian Xiaoerbulake Formation in the Tarim Basin mostly occurs with primary sedimentary structures, regardless of outcrops or underground formations. The primary morphology of carbonate grains could be vaguely discernible even after complete dolomitization [12,14]. Owing to good resistance to compaction, these primary rock structures act as a solid rock framework to protect the porosity (residual primary pores and secondary pores formed by freshwater dissolution), transforming dolograinstone into porous dolostones, exhibiting satisfactory reservoir quality after dolomitization [83,86].

5.3.2. Effects of Anhydrite Cementation

Anhydrite cementation is the second most important diagenetic process in the Early Cambrian Xiaoerbulake Formation, following dolomitization. These anhydrites likely originated from the dehydration of gypsum in a burial environment [45,87]. Among the various anhydrite textures, the pore-filling and poikilotopic types play a key role in reservoir quality [64]. They fill bulk pores by spreading within dolograinstone and dolopackstone in a shallow burial environment and considerably decrease reservoir porosity and permeability [64]. Reactive transport simulations in a reflux system demonstrate that anhydrite cements that were related to replacement dolomitization could sharply decrease core plug porosity and considerably reduce porosity by up to 25% [88]. However, breccia and associated fracture porosity are common in anhydrite-bearing sections [73,83]. Breccia-associated fracture porosity caused by a short period of meteoric water-induced dissolution is the predominant type of effective porosity in the anhydrite-bearing dolomudstone reservoir [73]. Additionally, the late anhydrite dissolution is responsible for improving reservoir quality by dissolving most of the early anhydrite cementation and creating new pore spaces [84]. Figure 12G,H show that interparticle pores and moldic pores in oolitic dolostone are fully infilled (cemented) with anhydrite. Herein, anhydrite cementation may undermine reservoir quality.

6. Conclusions

This research involves an integrated analysis of cores, well cuttings, thin section castings, thin sections of core and cuttings and well logging data to study the facies, depositional environment and reservoir quality of the Early Cambrian Xiaoerbulake Formation in the Tarim Basin of Northwest China. The main conclusions are summarized below.

(1) Ten facies types were identified, including mixed siliciclastic–carbonate rock, crystalline dolostone, dolobindstone, dolomudstone, argillaceous dolostone, dolograinstone, anhydrite–salt rock, dolomitized micrite, peloidal grainstone and argillaceous limestone. These facies are distinguished by their thickness, color, texture, structure, grains, fossil type and argillaceous and sand concentration.

(2) Seven facies associations were determined based on ten facies and twenty-six representative types of facies associations. The facies association types indicate that the Early Cambrian Xiaoerbulake Formation in the Tarim Basin represents deposits formed on a ramp on which three depositional environments were developed, including an inner ramp, middle ramp and outer ramp. The inner ramp comprises the tidal flat facies association, lagoon facies association, sabkha facies association and high-energy shoal facies association; the middle ramp comprises the inter-shoal sea facies association and low-energy shoal facies association and the outer ramp mainly comprises the open-shelf facies association.

(3) Facies types, together with dolomitization and anhydrite cementation, are the major factors controlling reservoir quality in the Early Cambrian Xiaoerbulake Formation in the Tarim Basin. The inner ramp high-energy shoal facies association exhibits good reservoir quality, while the mid-ramp and outer ramp depositional environments demonstrate poor reservoir quality. The early dolomitization can partly protect primary porosity and make dolograinstone a high-quality reservoir. Herein, anhydrite

cementation may negatively impact reservoir quality owing to its precipitation in the pore system.

Author Contributions: Conceptualization, Y.Z., J.Z. (Jianfeng Zhang) and J.Z. (Jiankun Zhang); methodology, Y.Z. and J.Z. (Jiankun Zhang); investigation, Y.Z., J.Z. (Jianfeng Zheng) and J.Z. (Jiankun Zhang); data curation, Y.Z., X.L., J.L. and F.H.; writing—original draft preparation, Y.Z., X.L., G.Y. (Guang Yu), J.L., F.H. and G.Y. (Guo Yang); writing—review and editing, J.Z. (Jiankun Zhang); visualization, G.Y. (Gang Yu) and F.H.; supervision, Y.Z. and J.Z. (Jiankun Zhang); project administration, J.Z.(Jianfeng Zheng). All authors have read and agreed to the published version of the manuscript.

Funding: The research was co-funded by the CNPC (China National Petroleum Corporation) Scientific Research and Technology Development Project (Grant Nos. 2021DJ0501, 2021DJ1501), Jiangxi Provincial Natural Science Foundation (No. 20202BAB204035) and Jiangxi Engineering Technology Research Center of Nuclear Geoscience Data Science and System (Grant Nos. JETRCNGDSS202103, JETRCNGDSS202002).

Data Availability Statement: Not applicable.

Acknowledgments: We deeply appreciate two anonymous reviewers and the editor for remarkable constructive comments that significantly improved the manuscript.

Conflicts of Interest: The authors declare no conflict of interest.

References

1. Burchette, T.P.; Wright, V.P. Carbonate ramp depositional systems. *Sediment. Geol.* **1992**, *79*, 3–57. [CrossRef]
2. Ahr, W.M. The carbonate remp: An alternative to the shelf model. *Trans. Gulf Coast Assoc. Geol. Soc.* **1973**, *23*, 221–225.
3. Wright, V.P. Facies sequences on a carbonate ramp: The Carboniferous Limestone of South Wales. *Sedimentology* **1986**, *33*, 221–241. [CrossRef]
4. Read, J.F. Carbonate Platform Facies Models. *AAPG Bull.* **1985**, *69*, 1–21.
5. Bábek, O.; Kalvoda, J.; Cossey, P.; Šimíček, D.; Devuyst, F.X.; Hargreaves, S. Facies and petrophysical signature of the Tournaisian/Viséan (Lower Carboniferous) sea-level cycle in carbonate ramp to basinal settings of the Wales-Brabant massif, British Isles. *Sediment. Geol.* **2013**, *284–285*, 197–213. [CrossRef]
6. Kakemem, U.; Jafarian, A.; Husinec, A.; Adabi, M.H.; Mahmoudi, A. Facies, sequence framework, and reservoir quality along a Triassic carbonate ramp: Kangan Formation, South Pars Field, Persian Gulf Superbasin. *J. Pet. Sci. Eng.* **2021**, *198*, 108166. [CrossRef]
7. Zou, C.; Du, J.; Xu, C.; Wang, Z.; Zhang, B.; Wei, G.; Wang, T.; Yao, G.; Deng, S.; Liu, J.; et al. Formation, distribution, resource potential, and discovery of Sinian–Cambrian giant gas field, Sichuan Basin, SW China. *Petrol. Explor. Dev.* **2014**, *41*, 306–325. [CrossRef]
8. Zhu, G.Y.; Huang, H.P.; Wang, H.T. Geochemical Significance of Discovery in Cambrian Reservoirs at Well ZS1 of the Tarim Basin, Northwest China. *Energy Fuels* **2015**, *29*, 1332–1344. [CrossRef]
9. Trippetta, F.; Durante, D.; Lipparini, L.; Romi, A.; Brandano, M. Carbonate-ramp reservoirs modelling best solutions: Insights from a dense shallow well database in Central Italy. *Mar. Pet. Geol.* **2021**, *126*, 104931. [CrossRef]
10. Tomassetti, L.; Petracchini, L.; Brandano, M.; Trippetta, F.; Tomassi, A. Modeling lateral facies heterogeneity of an upper Oligocene carbonate ramp (Salento, southern Italy). *Mar. Pet. Geol.* **2018**, *96*, 254–270. [CrossRef]
11. Du, J.H.; Pan, W.Q. Accumulation conditions and play targets of oil and gas in the Cambrian subsalt dolostone, Tarim Basin, NW China. *Petrol. Explor. Dev.* **2016**, *45*, 1111–1126. (In Chinese with English Abstract)
12. Zhu, Y.J.; Shen, A.J.; Liu, L.L.; Chen, Y.Q.; Yu, G. Tectonic-sedimentary filling history through the Later Sinian to the Mid-Cambrian in Tarim Basin and its explorational potential. *Acta Sediment. Sin.* **2020**, *38*, 398–410. (In Chinese with English Abstract)
13. Ma, Y.S.; Li, M.W.; Cai, X.Y.; Xu, X.H.; Hu, D.F.; Qu, S.L.; Li, G.S.; He, D.F.; Xiao, X.M.; Zeng, Y.J.; et al. Mechanisms and exploitation of deep marine petroleum accumulations in China: Advances, technological bottlenecks and basic scientific problems. *Oil Gas Geol.* **2020**, *41*, 655–672+683. (In Chinese with English Abstract)
14. Zhu, Y.J.; Ni, X.F.; Liu, L.L.; Qiao, Z.F.; Chen, Y.Q.; Zheng, J.F. Depositional differentiation and reservoir potential and distribution of ramp systems during post-rift period: An example from the Lower Cambrian Xiaoerbulake Formation in the Tarim Basin, NW China. *Acta Sediment. Sin.* **2019**, *37*, 1044–1057. (In Chinese with English Abstract)
15. Zheng, J.F.; Zhu, Y.J.; Huang, L.L.; Yang, G.; Hu, F.J. Geochemical Characteristics and Their Geological Significance of Lower Cambrian Xiaoerblak Formation in Northwestern Tarim Basin, China. *Minerals* **2022**, *12*, 781. [CrossRef]
16. He, Z.L.; Ma, Y.S.; Zhu, D.Y.; Duan, T.Z.; Geng, J.H.; Zhang, J.T.; Ding, Q.; Qian, Y.X.; Wo, Y.J.; Gao, Z.Q. Theoretical and technological progress and research direction of deep and ultra-deep carbonate reservoirs. *Oil Gas Geol.* **2021**, *42*, 533–546. (In Chinese with English Abstract)

17. Brandano, M.; Tomassetti, L.; Trippetta, F.; Ruggieri, R. Facies Heterogeneities and 3D Porosity Modelling in an Oligocene (Upper Chattian) Carbonate Ramp, Salento Peninsula, Southern Italy. *J. Pet. Geol* **2020**, *43*, 191–208. [CrossRef]
18. Bai, Y.; Luo, P.; Zhou, C.M.; Zhai, Z.G.; Wang, S.; Yang, Z.Y.; Wang, S. Sequence division and platform sedimentary evolution model of the Lower Cambrian Xiaoerbulak Formation in the NW Tarim Basin. *Oil Gas Geol.* **2017**, *38*, 152–164. (In Chinese with English Abstract)
19. Hu, M.Y.; Sun, C.Y.; Gao, D. Characteristics of tectonic-lithofacies paleogeography in the Lower Cambrian Xiaoerbulake Formation, Tarim Basin. *Oil Gas Geol.* **2019**, *40*, 12–23. (In Chinese with English Abstract)
20. Zheng, J.F.; Yuan, W.F.; Huang, L.L.; Pan, W.Q.; Qiao, Z.F.; Yang, G. Sedimentary facies model and its exploration significance of the Lower Cambrian Xiaoerblak Formation in Xiaoerblak area, Tarim Basin. *J. Palaeogeogr.* **2019**, *21*, 589–602. (In Chinese with English Abstract)
21. Zheng, J.F.; Huang, L.L.; Yuan, W.F.; Zhu, Y.J.; Qiao, Z.F. Geochemical features and its significance of sedimentary and diageneti-cenvironment in the Lower Cambrian Xiaoerblak Formation of Keping area, Tarim Basin. *Nat Gas Geosci.* **2020**, *31*, 698–709. (In Chinese with English Abstract)
22. Pan, W.Q.; Chen, Y.Q.; Xiong, Y.X.; Li, B.H.; Xiong, R. Sedimentary facies research and implications to advantaged exploration regions on Lower Cambrian source rocks, Tarim basin. *Oil Gas Geol.* **2015**, *26*, 1224–1232. (In Chinese with English Abstract)
23. Zhu, D.; Meng, Q.; Jin, Z.; Liu, Q.; Hu, W. Formation mechanism of deep Cambrian dolomite reservoirs in the Tarim basin, northwestern China. *Mar. Pet. Geol.* **2015**, *59*, 232–244. [CrossRef]
24. He, D.F.; Jia, C.Z.; Li, D.S.; Zhang, C.J.; Meng, Q.R.; Shi, X. Formation and evolution of polycyclic superimposed Tarim Basin. *Oil Gas Geol.* **2005**, *26*, 64–77. (In Chinese with English Abstract)
25. Wei, G.; Zhu, Y.; Zheng, J.; Yu, G.; Ni, X.; Yan, L.; Tian, L.; Huang, L. Tectonic-lithofacies paleogeography, large-scale source-reservoir distribution and exploration zones of Cambrian subsalt formation, Tarim Basin, NW China. *Petrol. Explor. Dev.* **2021**, *48*, 1289–1303. [CrossRef]
26. Wu, L.; Guan, S.W.; Feng, X.Q.; Ren, R.; Zhang, C.Y. Discussion on stratigraphic division of the Nanhuan and Sinian of the Tarim Basin and its surrounding region. *Acta Petrol. Sin.* **2020**, *36*, 3427–3441. (In Chinese with English Abstract)
27. Shi, K.B.; Liu, B.; Tian, J.C.; Pan, W.Q. Sedimentary characteristics and lithofacies paleogeography of Sinian in Tarim Basin. *Acta Pet. Sin.* **2016**, *37*, 1343–1360. (In Chinese with English Abstract)
28. Zhu, Y.J.; Zheng, J.F.; Cao, P.; Qiao, Z.F.; Yu, G.; Liu, L.L.; Huang, L.L. Tectonic-Lithofacies Paleogeography and Sizeable Reservoir Potential in the Early Cambrian Postrift Depressed Carbonate Ramp, Tarim Basin, NW China. *Lithosphere* **2021**, *2021*, 8804537. [CrossRef]
29. Wang, Z.; Gao, Z.; Fan, T.; Shang, Y.; Qi, L.; Yun, L. Structural characterization and hydrocarbon prediction for the SB5M strike-slip fault zone in the Shuntuo Low Uplift, Tarim Basin. *Mar. Pet. Geol.* **2020**, *117*, 104418. [CrossRef]
30. Deng, S.; Liu, Y.Q.; Liu, J.; Han, J.; Wang, B.; Zhao, R. Structural styles and evolution models of intracratonic strike-slip faults and the implications for reservoir exploration and appraisal: A case study of the Shunbei area, Tarim Basin. *Geotect Metal.* **2020**, *45*, 1111–1126. (In Chinese with English Abstract)
31. Folk, R.L. Practical Petrographic Classification of Limestones. *AAPG Bull.* **1959**, *43*, 1–38.
32. Dunham, R.J. Classification of carbonate rocks according to their depositional texture. In *Classification of Carbonate Rocks (AAPG Memoir 1)*; Ham, W.E., Ed.; American Association of Petroleum Geologists: Tulsa, OK, USA, 1962; pp. 108–121.
33. Flügel, E. *Microfacies of Carbonate Rocks: Analysis, Interpretation and Application*, 2nd ed.; Springer: New York, NY, USA, 2010; pp. 73–900.
34. Friedman, G.M. Terminology of crystallization textures and fabrics in sedimentary rocks. *J. Sediment. Res.* **1965**, *35*, 643–655.
35. Sibley, D.F.; Gregg, J.M. Classification of dolomite rock textures. *J. Sediment. Res.* **1987**, *57*, 967–975.
36. Wilson, J.L. *Carbonate Facies in Geologic History*; Springer: Berlin, Heidelberg; New York, NY, USA, 1975; pp. 20–347.
37. Lucia, F.J. Rock-Fabric/Petrophysical Classification of Carbonate Pore Space for Reservoir Characterization. *AAPG Bull.* **1995**, *79*, 1275–1300.
38. Wu, F.; Xie, X.; Zhu, Y.; Coletti, G.; Betzler, C.; Cui, Y.; Bai, H.; Chen, B.; Shang, Z. Early development of carbonate platform (Xisha Islands) in the northern South China Sea. *Mar. Geol.* **2021**, *441*, 106629. [CrossRef]
39. Christiano-De-Souza, I.; Ricardi-Branco, F.; Silva, A.; El-Dash, L.; Faria, R. New approach for the study of paleofloras using geographical information systems applied to Glossopteris Flora. *Braz. J. Geol.* **2014**, *44*, 681–689. [CrossRef]
40. Ng, C.; Vega, C.S.; Maranhão, M.d.S.A.S. Mixed carbonate-siliciclastic microfacies from Permian deposits of Western Gondwana: Evidence of gradual marine to continental transition or episodes of marine transgression? *Sediment. Geol.* **2019**, *390*, 62–82. [CrossRef]
41. Rivers, J.M.; Dalrymple, R.W.; Yousif, R.; Al-Shaikh, I.; Butler, J.D.; Warren, C.; Skeat, S.L.; Bari, E. Mixed siliciclastic-carbonate-evaporite sedimentation in an arid eolian landscape: The Khor Al Adaid tide-dominated coastal embayment, Qatar. *Sediment. Geol.* **2020**, *408*, 105730. [CrossRef]
42. Farouk, S.; Al-Kahtany, K.; Tawfik, M. Upper Cretaceous (Coniacian -Campanian) siliciclastic/carbonate ramp depositional sequences and relative sea-level changes in Sinai, Egypt: Implications from facies analysis. *Mar. Pet. Geol.* **2021**, *131*, 105183. [CrossRef]
43. Halfar, J.; Ingle, J.C.; Godinez-Orta, L. Modern non-tropical mixed carbonate-siliciclastic sediments and environments of the southwestern Gulf of California, Mexico. *Sediment. Geol.* **2004**, *165*, 93–115. [CrossRef]

44. Zhang, Y.; Pan, W.; Zhu, B.; Li, W.; Yang, L.W.; Chen, Y.; Yang, T. Recrystallization of dolostones in the Cambrian Xiaoerbrak Formation, Tarim Basin and possible link to reservoir development. *Mar. Pet. Geol.* **2022**, *136*, 105452. [CrossRef]
45. Testa, G.; Lugli, S. Gypsum–anhydrite transformations in Messinian evaporites of central Tuscany (Italy). *Sediment. Geol.* **2000**, *130*, 249–268. [CrossRef]
46. Huang, S.J.; Yang, J.J.; Zhang, W.Z.; Huang, Y.M.; Liu, C.X.; Xiao, L.P. Effects of gypsum (or anhydrite) on dissolution of dolomite under different temperatures and pressures of epigenesis and burial diagenesis. *Acta Sediment. Sin.* **1996**, *14*, 103–109. (In Chinese with English Abstract)
47. Murray, R.C. Origin and diagenesis of gypsum and anhydrite. *J. Sediment. Res.* **1964**, *34*, 512–523.
48. Shinn, E.A. Practical significance of birdseye structures in carbonate rocks. *J. Sediment. Res.* **1968**, *38*, 215–223. [CrossRef]
49. Xu, L.; Chen, T.H.; Gao, Y.; Chen, P.; Xie, Q.Q.; Zhou, Y.F. Genesis of bird's-eye structure in the Triassic Dongmaanshan Formation in Chaohu, Anhui Province. *Earth Sci. Front.* **2020**, *27*, 294–301. (In Chinese with English Abstract)
50. Riding, R. Microbialites, stromatolites, and thrombolites. In *Encyclopedia of Geobiology (Encyclopedia of Earth Sciences Series)*; Reitner, J., Thiel, V., Eds.; Springer: Dordrecht, The Netherlands, 2011; pp. 635–654.
51. Zhang, Y.; Li, J.; Chen, L.; Wei, Y.; Shi, Q.; Wang, D.; Wu, Q.; Song, L.; Tian, M.; Kuang, H.; et al. Manganese carbonate stromatolites of the Ediacaran Doushantuo Formation in Chengkou, northern Yangtze Craton, China. *J. Palaeogeogr.* **2021**, *10*, 356–381. [CrossRef]
52. Pruss, S.B.; Knoll, A.H. Environmental covariation of metazoans and microbialites in the Lower Ordovician Boat Harbour Formation, Newfoundland. *Palaeogeogr. Palaeoclimatol. Palaeoecol.* **2017**, *485*, 917–929. [CrossRef]
53. Amel, H.; Jafarian, A.; Husinec, A.; Koeshidayatullah, A.; Swennen, R. Microfacies, depositional environment and diagenetic evolution controls on the reservoir quality of the Permian Upper Dalan Formation, Kish Gas Field, Zagros Basin. *Mar. Pet. Geol.* **2015**, *67*, 57–71. [CrossRef]
54. Yang, W.; Li, P.; Chen, H.; Liu, Z.; Lan, C.; Xu, Z.; Lu, C.; Zou, H. Origin and significance of carbonate shoal depositional cycles: A case study of the Cambrian Longwangmiao Formation, Sichuan Basin, SW China. *J. Asian Earth Sci.* **2022**, *226*, 105083. [CrossRef]
55. Wang, Z.M.; Xie, H.W.; Chen, Y.Q.; Qi, Y.M.; Zhang, K. Discovery and exploration of Cambrian subsalt dolostone original hydrocarbon reservoir at Zhongshen-1 Well in Tarim Basin. *China Pet. Explor.* **2014**, *19*, 1–13. (In Chinese with English Abstract)
56. Hu, M.; Gao, D.; Wei, G.; Yang, W.; Xie, W. Sequence stratigraphy and facies architecture of a mound-shoal-dominated dolomite reservoir in the late Ediacaran Dengying Formation, central Sichuan Basin, SW China. *Geol. J.* **2019**, *54*, 1653–1671. [CrossRef]
57. Riera, R.; Bourget, J.; Allan, T.; Hakansson, E.; Wilson, M.E.J. Early Miocene carbonate ramp development in a warm ocean, North West Shelf, Australia. *Sedimentology* **2022**, *69*, 219–253. [CrossRef]
58. Pettijohn, F.J.; Potter, P.E.; Siever, R. *Sand and Sandstone*; Springer: Berlin, Germany, 1972; pp. 1–618.
59. Li, F.; Yan, J.X.; Chen, Z.Q.; Ogg, J.G.; Tian, L.; Korngreen, D.; Liu, K.; Ma, Z.L.; Woods, A.D. Global oolite deposits across the Permian-Triassic boundary: A synthesis and implications for palaeoceanography immediately after the end-Permian biocrisis. *Earth Sci. Rev.* **2015**, *149*, 163–180. [CrossRef]
60. Corsetti, F.A.; Kidder, D.L.; Marenco, P.J. Trends in oolite dolomitization across the Neoproterozoic–Cambrian boundary: A case study from Death Valley, California. *Sediment. Geol.* **2006**, *191*, 135–150. [CrossRef]
61. Zempolich, W.G.; Baker, P.A. Experimental and natural mimetic dolomitization of aragonite ooids. *J. Sediment. Res.* **1993**, *63*, 596–606.
62. Osburn, M.; Grotzinger, J.; Bergmann, K. Facies, stratigraphy, and evolution of a middle Ediacaran carbonate ramp: Khufai Formation, Sultanate of Oman. *AAPG Bull.* **2014**, *98*, 1631–1667. [CrossRef]
63. Strasser, A. Ooids in Purbeck limestones (lowermost Cretaceous) of the Swiss and French Jura. *Sedimentology* **1986**, *33*, 711–727. [CrossRef]
64. Jafarian, A.; Fallah-Bagtash, R.; Mattern, F.; Heubeck, C. Reservoir quality along a homoclinal carbonate ramp deposit: The Permian Upper Dalan Formation, South Pars Field, Persian Gulf Basin. *Mar. Pet. Geol.* **2017**, *88*, 587–604. [CrossRef]
65. Duringer, P.; Vecsei, A. Middle Triassic shallow-water limestones from the Upper Muschelkalk of eastern France: The origin and depositional environment of some early Mesozoic fine-grained limestones. *Sediment. Geol.* **1998**, *121*, 57–70. [CrossRef]
66. Liu, Y.; Hu, M.; Zhang, S.; Zhang, J.; Gao, D.; Xiao, C. Characteristics and impacts on favorable reservoirs of carbonate ramp microfacies: A case study of the Middle—Lower Ordovician in Gucheng area, Tarim Basin, NW China. *Petrol. Explor. Dev.* **2022**, *49*, 107–120. [CrossRef]
67. Badenas, B.; Aurell, M.; Gasca, J.M. Facies model of a mixed clastic-carbonate, wave-dominated open-coast tidal flat (Tithonian-Berriasian, north-east Spain). *Sedimentology* **2018**, *65*, 1631–1666. [CrossRef]
68. Ismail, M.J.; Ettensohn, F.R.; Handhal, A.M.; Al-Abadi, A. Facies analysis of the Middle Cretaceous Mishrif Formation in southern Iraq borehole image logs and core thin-sections as a tool. *Mar. Pet. Geol.* **2021**, *133*, 105324. [CrossRef]
69. Luan, X.C.; Brett, C.E.; Zhan, R.B.; Liu, J.B.; Wu, R.C.; Liang, Y. Microfacies analysis of the Lower-Middle Ordovician succession at Xiangshuidong, southwestern Hubei Province, and the drowning and shelf-ramp transition of a carbonate platform in the Yangtze region. *Paleogeogr. Paleoclimatol. Paleoecol.* **2017**, *485*, 68–83. [CrossRef]
70. Shen, A.; Zheng, J.; Chen, Y.; Ni, X.; Huang, L. Characteristics, origin and distribution of dolomite reservoirs in Lower-Middle Cambrian, Tarim Basin, NW China. *Petrol. Explor. Dev.* **2016**, *43*, 375–385. [CrossRef]

71. Choquette, P.W.; Pray, L.C. Geologic Nomenclature and Classification of Porosity in Sedimentary Carbonates. *AAPG Bull.* **1970**, *54*, 207–250.
72. Lønøy, A. Making sense of carbonate pore systems. *AAPG Bull.* **2006**, *90*, 1381–1405. [CrossRef]
73. Jiang, L.; Worden, R.H.; Cai, C.F.; Shen, A.J.; Crowley, S.F. Diagenesis of an evaporite-related carbonate reservoir in deeply buried Cambrian strata, Tarim Basin, northwest China. *AAPG Bull.* **2018**, *102*, 77–102. [CrossRef]
74. Lai, J.; Liu, S.C.; Xin, Y.; Wang, S.; Xiao, C.W.; Song, Q.Q.; Chen, X.; Yang, K.F.; Wang, G.W.; Ding, X.J. Geological-petrophysical insights in the deep Cambrian dolostone reservoirs in Tarim Basin, China. *AAPG Bull.* **2021**, *105*, 2263–2296. [CrossRef]
75. Friedman, G.M. Unconformities and Porosity Development in Carbonate Strata: Ideas from a Hedberg Conference: Discussion. *AAPG Bull.* **1995**, *79*, 1183–1184.
76. Zhu, G.Y.; Chen, Z.Y.; Chen, W.Y.; Yan, H.H.; Zhang, P.H. Revisiting to the Neoproterozoic tectonic evolution of the Tarim Block, NW China. *Precambrian Res.* **2021**, *352*, 106013. [CrossRef]
77. Wu, G.H.; Li, Q.M.; Xiao, Z.R.; Li, H.H.; Zhang, L.P.; Zhang, X.J. The Evolution Characteristics of Palaeo-Uplifts in Tarim Basin and Its Exploration Directions for Oil and Gas. *Geotect Metal.* **2009**, *33*, 124–130. (In Chinese with English Abstract)
78. Chen, Y.Q.; Yan, W.; Han, C.W.; Yang, T.F.; Li, Z. Redefinition on structural paleogeography and lithofacies paleogeography framework from Cambrian to Early Ordovician in the Tarim Basin: A new approach based on seismic stratigraphy evidence. *Nat Gas Geosci.* **2015**, *26*, 1832–1843. (In Chinese with English Abstract)
79. Yan, W.; Wu, G.H.; Zhang, Y.Q.; Yang, G.; Lou, H.; Wang, X.M. Sinian-Cambrian tectonic framework in the Tarim Basin and its influences on the paleogeography of the Early Cambrian. *Geotect Metal.* **2018**, *42*, 455–466. (In Chinese with English Abstract)
80. Ouyang, S.Q.; Lyu, X.X.; Xue, N.; Li, F.; Wang, R. Paleoenvironmental characteristics and source rock development model of the Early-Middle Cambrian: A case of the Keping-Bachu area in the Tarim Basin. *J. China Univ. Min. Technol.* **2022**, *51*, 293–310. (In Chinese with English Abstract)
81. Zhang, C.Y.; Guan, S.W.; Wu, L.; Ren, R.; Xiong, L.Q. Geochemical characteristics and its paleo-environmental significance of the Lower Cambrian carbonate in the northwestern Tarim Basin: A case study of Well Shutan-1. *Bull. Geol. Sci. Technol.* **2021**, *40*, 99–111. (In Chinese with English Abstract)
82. Gao, D.; Hu, M.Y.; Li, A.P.; Yang, W.; Xie, W.R.; Sun, C.Y. High-frequency sequence and microfacies and their impacts on favorable reservoir of Longwangmiao Formation in Central Sichuan Basin. *Earth Sci.* **2021**, *46*, 3520–3534. (In Chinese with English Abstract)
83. Jiang, L.; Cai, C.; Worden, R.H.; Crowley, S.F.; Jia, L.; Zhang, K.; Duncan, I.J. Multiphase dolomitization of deeply buried Cambrian petroleum reservoirs, Tarim Basin, north-west China. *Sedimentology* **2016**, *63*, 2130–2157. [CrossRef]
84. Mohammed-Sajed, O.K.; Glover, P.W.J. Influence of anhydritisation on the reservoir quality of the Butmah Formation in north-western Iraq. *Mar. Pet. Geol.* **2022**, *135*, 105391. [CrossRef]
85. Jiang, L.; Xu, Z.H.; Shi, S.Y.; Liu, W. Multiphase dolomitization of a microbialite-dominated gas reservoir, the middle Triassic Leikoupo Formation, Sichuan Basin, China. *J. Pet. Sci. Eng.* **2019**, *180*, 820–834. [CrossRef]
86. Zhao, W.Z.; Shen, A.J.; Zheng, J.F.; Qiao, Z.F.; Wang, X.F.; Lu, J.M. The porosity origin of dolostone reservoirs in the Tarim, Sichuan and Ordos basins and its implication to reservoir prediction. *Sci. China-Earth Sci.* **2014**, *57*, 2498–2511. [CrossRef]
87. Hardie, L.A. The Gypsum–anhydrite equilibrium at one atmosphere pressure. *Am. Mineral.* **1967**, *52*, 171–200.
88. Jones, G.D.; Xiao, Y. Dolomitization, anhydrite cementation, and porosity evolution in a reflux system: Insights from reactive transport models. *AAPG Bull.* **2005**, *89*, 577–601. [CrossRef]

Disclaimer/Publisher's Note: The statements, opinions and data contained in all publications are solely those of the individual author(s) and contributor(s) and not of MDPI and/or the editor(s). MDPI and/or the editor(s) disclaim responsibility for any injury to people or property resulting from any ideas, methods, instructions or products referred to in the content.